AGU ADVANCING EARTH AND SPACE SCIENCE

Water Resources Research

RESEARCH ARTICLE
10.1029/2020WR027893

# The Use of Rain Gauge Measurements and Radar Data for the Model-Based Prediction of Runoff-Generated Debris-Flow Occurrence in Early Warning Systems

**Martino Bernard**[1] and **Carlo Gregoretti**[1]

[1]Land Environment Agriculture and Forestry Department, University of Padova, Legnaro, Padova, Italy

**Key Points:**

- In the last decade several debris flows have been triggered in the highly tourist Boite Valley
- Rain gauge and radar recorded rainfalls have been used to simulate debris-flow triggering discharges
- In this area radar needs the presence of rain gauges to be used in early warning systems

**Supporting Information:**

- Supporting Information S1
- Figure S1
- Figure S2

**Correspondence to:**
M. Bernard,
martino.bernard@unipd.it

**Citation:**
Bernard, M., & Gregoretti, C. (2021). The use of rain gauge measurements and radar data for the model-based prediction of runoff-generated debris-flow occurrence in early warning systems. *Water Resources Research*, *57*, e2020WR027893. https://doi.org/10.1029/2020WR027893

Received 12 MAY 2020
Accepted 14 JAN 2021



**Abstract** High-intensity and short-duration rainfalls can generate sudden and abundant runoff at the base of rocky cliffs that, entraining sediments, may originate debris flows. Two gauge networks have been set up in headwater sites of Dolomites (Northeastern Italian Alps) to monitor rainfall corresponding to the debris-flow activity occurring there. The rain gauges are positioned both upstream and downstream the initiation areas of debris flows. Other five rain gauges sparse in the area integrate the two networks. In the years 2009–2020, rain gauges recorded rainfalls that triggered 41 debris flows. In most cases, rainfalls show a higher spatial variability along with both distance and altitude. Precipitation data are then compared with rainfalls estimated through a weather radar far about 70 km from there, to verify the possible interchangeability of the two measurement systems for the prediction of debris-flow occurrence through suitable modeling of triggering discharges. The following results are obtained: (1) raw-radar images mostly tend to underestimate precipitations recorded by rain gauges; (2) such underestimation entails, on average, a larger one on the simulated discharges and the prediction of debris-flow occurrences (missed in 65% of the cases). Some methods for the correction on ground truth of raw-radar images are applied to assess their use for evaluating the triggering discharges. Results show that once corrected using rain gauge data, radar-derived rainfall estimates produce debris-flow initiation predictions that more frequently match observations. Therefore, the presence of rain gauges close to the watershed centroids results essential for early warning systems based on triggering discharge modeling.

## 1. Introduction

Debris flows (DFs) are classified as mixtures of sediments and water that rapidly route along steep channels. In mountainous regions, the impulsive nature of DFs combined with their high devastating power threatens human life and facilities (Jakob & Hungr, 2005) and has a high socioeconomic impact (Thiene et al., 2017). In this work, we refer to runoff-generated DFs, that is, those formed after the entrainment of debris material into abundant runoff descending from rocky cliffs (Coe et al., 2008; Hürlimann et al., 2014; Kean et al., 2013). Doubtless, high-intensity and sub-hourly rainfalls (15–45 minutes) are the predominant factors for the triggering and magnitude of runoff generated DFs.

The prediction of such phenomena has great relevance for limiting damages and victims in the threatened areas and increasingly enters the context of social challenges. Many villages, tourist resorts, and linear infrastructures are built on DF fans or intersect DF channels. The expansion of human activities (new settlements, infrastructures, and touristic facilities, often in the extreme alpine environment) increases the vulnerability of society to these phenomena (Franceschinis et al., 2020). Moreover, the frequency of these phenomena is growing due to climate change (Stoffel et al., 2014); it leads to the increasing of both extreme rainfalls (Floris et al., 2010) and rock wall collapses that provide sediments even in locations where they never occurred before (Gatter et al., 2018; Bernard, Berti, et al., 2019). The large number of sites, which are potentially threatened, and the inherent inflexibility of technical countermeasures characterized by high costs make early warning systems the most cost-effective measure to mitigate the risk associated with DFs (Sättele et al., 2015). Because of the short times of DF downstream routing, the prediction of occurrences should occur as soon as possible. The real-time evaluation of triggering rainfalls permits to launch alerts in a time shorter than that given during DF downstream routing by sensors positioned along DF flow paths. The most common way to predict DF occurrences is the use of rainfall-based thresholds in early warning systems (Baum & Godt, 2010; Cannon et al., 2008; Palau et al., 2020; Restrepo et al., 2008). Following the

pioneers Caine (1980) and Innes (1983), considerable efforts have been made to identify local or regional critical thresholds: precipitations exceeding these limits should be able to generate discharges prone to initiate DFs. Despite the large number of works carried out (Guzzetti et al., 2008; Segoni et al., 2018 with the references therein), the employment of corresponding thresholds for forecasts or warnings is not entirely accurate. Limits of this approach are the sub-hourly spatial variability of convective rainfalls; the scarcity of historical event databases; the high variability of antecedent humidity conditions (Gregoretti & Dalla Fontana, 2007); the variations of environmental conditions during years (Papa et al., 2013); the site-dependence of evaluated thresholds (Staley et al., 2013). In the case of just burned watersheds, critical thresholds can be used with success in early warning systems. In these basins, the hydrologic properties of terrain surface are quite uniform and it is possible to find reliable spatially variable rainfall-intensity thresholds combining historical data and statistical methods for DF susceptibility (Staley et al., 2017). To overcome these problems, similarly to that done for flash floods (Borga et al., 2010), nowadays, it is explored the possibility of estimating thresholds through models that link rainfalls and triggering of DFs, for example, hydrological modeling of headwater basin response, infinite-slope stability models, etc. (e.g., Bathurst et al., 2006; Crosta & Frattini, 2003; McGuire & Youberg, 2020). For these reasons, rainfall fields need to be accurately recorded to be used for assessing debris-flow initiation by hydrological modeling (Destro et al., 2018).

DF triggering storms are influenced by the topography of mountainous areas, denoting a large gradient in the space (Marra et al., 2014). The rainfall field often exhibits a local peak in the proximity of the triggering zone (Nikolopoulos et al., 2014). To evaluate triggering rainfalls, rain gauges and weather radars are the more appropriate sources of information. The rain gauge-based estimation of triggering rainfalls is in general uncertain (Villarini et al., 2008): the distance of reference rain gauges from the initiation zones of DFs, both on the horizontal and on elevation, leads to an underestimation of the triggering rainfalls (Nikolopoulos et al., 2015). Moreover, the intergauges distance of regional monitoring networks is generally in the order of 5–10 km; thus, a trustworthy spatial estimation is hardly obtainable. This limitation could be overcome by utilizing weather radars (Cremonini & Tiranti, 2018). Radars do not directly measure the rainfall but record the energy reflected by any hit object in the atmosphere. Reflected energy is related to the radar reflectivity factor, $Z$, that is used to estimate rainfall rates, $R$, through a $Z$-$R$ relationship (Rendon et al., 2013). Radar-rainfall estimates denote high spatial and temporal resolutions, covering continuously the area of interest. Despite the rapid advance in knowledge about this technology, radar rainfall estimates are still affected by various uncertainty factors reducing their accuracy, especially in mountainous areas (Germann et al., 2006). Furthermore, DF watershed sizes are similar to the extension of a radar cell and the rainfall variability could not be detected. This shortcoming leads to a rainfall overestimation/underestimation depending on recording/not recording of the local peak of precipitations (Rabiei & Haberlandt, 2015). For these reasons, Krajewski et al. (2010) pointed out that, at the moment, the usage of dense rain gauge network is essential for having accurate precipitation measures and the best approach for providing optimal rainfall data becomes the merging of every available information (Delrieu et al., 2014).

Merged rainfall estimates can be used as input rainfalls for simulating both runoff and flood routing in mountainous areas (Borga et al., 2006; Cunha et al., 2012; Sapriza-Azuri et al., 2015; Tramblay et al., 2011; Uhlenbrook & Tetzlaff, 2006). Information of interest is both the rainfall measures (as punctual measurements and radar/satellite raw data) and the topographical characteristics (Goovaerts, 2000). To give more consistency to radar data, some correction methods need to be applied. These techniques are various and, each of them, with particular intrinsic errors (Hartkamp et al., 1999). The choice of which method is fundamental for the mountainous environment (Burrough & McDonnell, 1998), where sampling is scattered and information could differ substantially (Collins & Bolstad, 1996). Hasan et al. (2016) showed how increasing the complexity of merging algorithms the accuracy of results increases, provided that a sufficient number of rain gauge observations are available.

In this work, we compare rainfall measured by rain gauges with radar-derived rainfall estimates. The objective is to understand how differences in rainfall estimates during DF-producing storms translate into differences in modeled discharge, with a particular emphasis on whether or not the modeled discharge exceeds established thresholds for DF initiation. This is a first step in the process of exploring the possible use of rain gauge and/or radar data, in combination with a hydrologic model, in early warning systems for the real-time

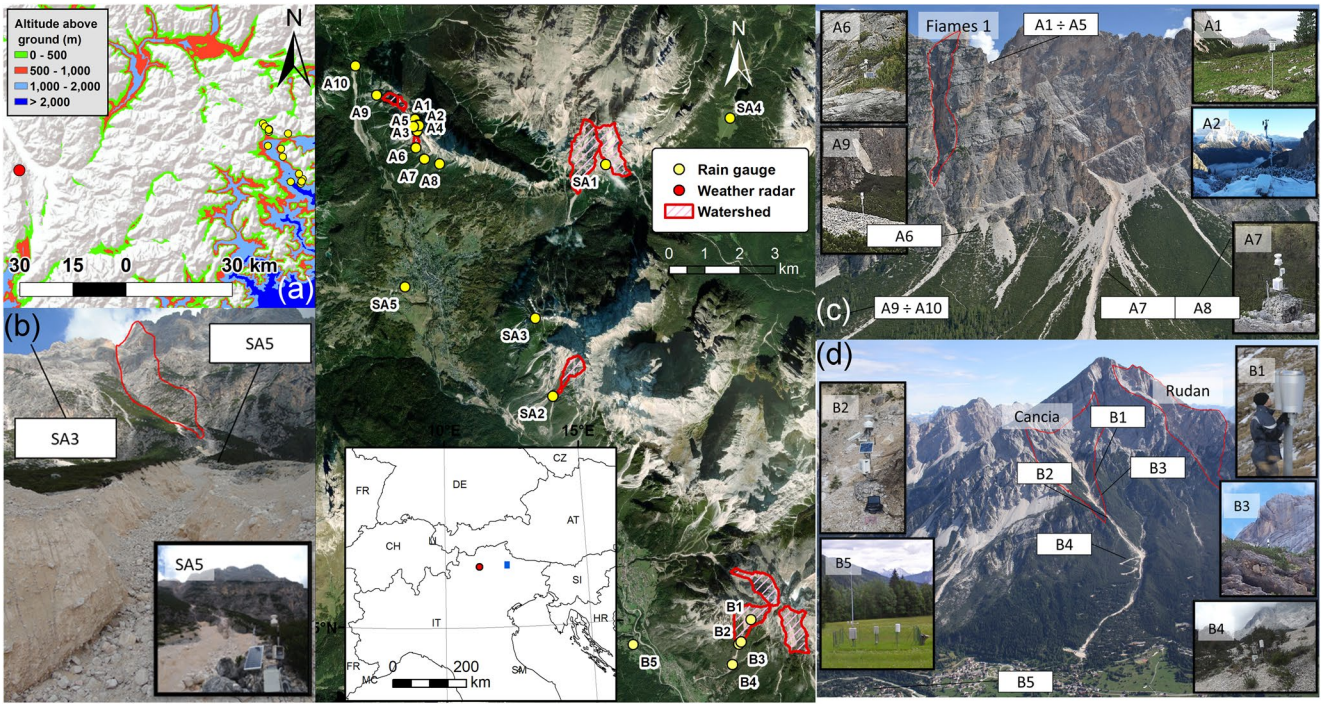


**Figure 1.** Aerial view of the study area. Boundaries of the considered watershed are denoted by a red line, and the rain gauges by a yellow dot. Panel (a) shows the elevation of the vertical profile above the ground not covered by the radar beam; in (b), the Punta Nera basin. In the panels (c) and (d), the frontal views of the Fiames monitoring site, and the Cancia one. Each insert shows some of the rain gauges present in the area. The labels indicate their locations.

evaluation of DF occurrence. A second step is the assessment of DF occurrence timing. For operational use, it should be closer to the observed one. In this way, the alert time for implementing the safety procedures (as closing roads and/or population evacuation, when necessary) should be enough. The prerequisite for using models in DF early warning systems is, in fact, their reliability, robustness, and short running time. More in detail, the objective is to understand how different estimates of rainfalls that triggered occurred DFs influence the simulation of the corresponding runoff. Once substantial differences have been found, we additionally searched for the easier methodology to adjust radar estimates for the purpose of improving the modeling outcomes. Therefore, the goal is not the development of algorithms for the correction of radar maps, but the use of radar estimates aimed at modeling DFs triggering. The remainder of the paper is organized as follows: Section 2 presents the study area and the rainfall data set. Section 3 illustrates the implemented methodologies for correcting radar images, the hydrological model and the rainfall Scenarios used for the hydrological modeling. Section 4 contains results and the corresponding discussion. Finally, a summary of the work is provided in Section 5.

## 2. Study Site

### 2.1. Study Area and DF Basins

The DF events analyzed in this study occurred along the left side of the Boite river valley in the Dolomites area of the Italian Alps (north-eastern Italy). In this area, old and recent occurrences of landslides are evident. In summer, the local population and productive activities are exposed to serious socioeconomic risks due to DF phenomena. They often cause fatalities, homelessness, and road interruptions, damaging the main local economy, which is mainly based on national and international tourism (Mattea et al., 2016). Figure 1 shows the whole study area, ~300 $km^2$.

The domain is characterized by a complex topography. Elevation ranges between 900 and 3,250 m a.s.l., with a mean altitude of about 1,850 m a.s.l. The landscape is dominated by large dolomite massifs: bedrock outcrops occupy large areas of the basins, mainly above 1,800 m a.s.l. where vegetation is limited

**Table 1**
*Watersheds With at Least One Occurred Debris Flow Since 2009. $\theta_{slope}$ Refers to the Basin Average Slope Angle, B, $\theta_{trig}$, and $d_M$ Refer to Bottom Width, Mean Diameter of Sediments and Channel Slope Angle at the Triggering section*

| Watershed | Area ($km^2$) | $\theta_{slope}$ (°) | B (m) | $\theta_{trig}$ (°) | $d_M$ (m) | $Q_{CRIT}$ ($m^3/s$) | LiDAR data |
|---|---|---|---|---|---|---|---|
| Fiames 1[a] | 0.03 | 72.3 | 2.20 | 33 | 0.09 | 0.17 | LiDAR 2011 |
| Fiames 2[b] | 0.15 | 68.5 | 4.10 | 28 | 0.13 | 0.33 | LiDAR 2011 |
| Punta Nera[a] | 0.20 | 51.5 | 5.00 | 22 | 0.04 | 0.11 | LiDAR 2010 |
| Rio Gere[a] | 1.07 | 54.6 | 5.00 | 26 | 0.05 | 0.35 | LiDAR 2010 |
| Rovina di Cancia[b] | 0.65 | 54.2 | 8.00 | 27 | 0.07 | 0.68 | LiDAR 2011 |
| Rudan[b] | 0.71 | 66.7 | 3.00 | 31 | 0.07 | 0.18 | LiDAR 2011 |
| Rudavoi[a] | 0.75 | 47.7 | 3.50 | 29 | 0.05 | 0.24 | LiDAR 2010 |
| Ru Secco[a] | 0.57 | 55.4 | 3.0 | 23 | 0.1 | 0.478 | LiDAR 2015 |

*Note*. $Q_{CRIT}$ is the DF triggering critical discharge distinctive for each basin evaluated by the Equation 10.
[a]Present work survey data. [b]Survey data from Gregoretti and Dalla Fontana (2008).

and sub-vertical rock cliffs are prevalent (Marchi et al., 2008). At the base of steep rock cliffs, scree slopes represent sources of abundant debris. Taluses are made of poorly sorted sediments, ranging from particles to boulders. In this area, DFs generally initiate following high-intensity convective rainfall events (Gregoretti & Dalla Fontana, 2007). Headwater rocky basins rapidly deliver high discharges at the outlet that can mobilize loose channel-bed sediments (Berti et al., 2020). The mobilization of loose materials has been well documented in the past, by both field monitoring (Berti & Simoni, 2005; Tecca & Genevois, 2009) and postevent field surveys (D'Agostino et al., 2010; Gregoretti & Dalla Fontana, 2008; Pastorello et al., 2020; Simoni et al., 2020). DF magnitude depends on sediment availability and runoff volume. It is generally enhanced by the entrainment of bed sediments during the propagation (Berger et al., 2010; Reid et al., 2016), and mitigated by the control works built along the channel (Bernard, Boreggio et al., 2019; Piton & Recking, 2016) if existing. The routing of these phenomena ends on the valley bottom, threatening the national road 51 and the settlements built around it (Thiene et al., 2017). The earliest documented occurred DFs date back to the second half of the 19th century (D'Agostino & Marchi, 2001). Events analyzed in this work are those that occurred after 2006 because radar data were not available before. The presence of rain gauges nearby the different initiation areas is fundamental to obtain the truthful triggering rainfall depth. Otherwise, precipitations have to be estimated through the rain gauges managed by the Regional Agency for Environmental Prevention and Protection of Veneto (ARPAV), 1–5.5 km far from triggering areas (Gregoretti & Dalla Fontana, 2008).

In the study area shown in Figure 1, we recognize eight basins subjected to DF activity, two of which in the area of Fiames. The basins (closed in correspondence of the DF initiation area) are listed in Table 1 with their morphological characteristics and hydrologic and topographical data. DFs initiate just below the base of the rocky cliffs but two cases: in the case of the Punta Nera basin, the DF initiation occurs on a chute incising the rocky cliffs where debris material deposited after a cliff collapse (Bernard, Berti et al., 2019); in the case of the Rovina di Cancia basin, it occurs rather downstream the base of rocky cliffs because the upper part of the incised channel is occupied by several giant boulders that prevent the formation of consistent DF surges (Bernard, Boreggio et al., 2019; Simoni et al., 2020). However, in any case, the largest contribution to surface runoff comes from the rock walls. The geometric features of the watersheds (i.e., the area and the average slope angle $\theta_{slope}$) have been computed employing DEMs (1-m grid size) derived from three LiDAR surveys carried out in 2010 (1 point/$m^2$ density), 2011 (3 points/$m^2$), and 2015 (10 points/$m^2$). These LiDAR data were provided by the association "Regole d'Ampezzo," the Land Protection Service of the province of Belluno (LPSB), and the Department of Public Works of the Veneto Region respectively (in Table 1, for each basin, LiDAR data used for building corresponding DEMs are reported). The morphology and the sediment characteristics of each initiation zone, such as the bottom width, the longitudinal slope angle $\theta_{trig}$, and the mean grain size $d_M$, are those provided by Gregoretti and Dalla Fontana (2008) or have been directly determined in the field following their approach.

**Table 2**
*Rain Gauges Located in the Study Area*

| Rain gauge | East coordinate (m) | North coordinate (m) | Elevation (m a.s.l) | Working period | Managed by |
|---|---|---|---|---|---|
| A1 | 740,087 | 5,163,191 | 2,126 | Jul 2010 to present | UNI |
| A2 | 740,162 | 5,163,024 | 2,150 | Jun 2011 to present | UNI |
| A3[a] | 740,149 | 5,162,866 | 2,154 | Jun 2011 to present | UNI |
| A4 | 740,199 | 5,163,017 | 2,146 | Jun 2011 to present | UNI |
| A5 | 740,044 | 5,162,990 | 2,158 | Jun 2011 to present | UNI |
| A6[a] | 740,109 | 5,162,382 | 1707 | Jul 2010 to present | UNI |
| A7 | 740,339 | 5,162,058 | 1,659 | Jun 2014 to present | UNI |
| A8 | 740,781 | 5,161,932 | 1,692 | Jul 2009 to Nov 2015 | UNI |
| A9 | 738,994 | 5,163,875 | 1,518 | Jul 2013 to present | UNI |
| A10 | 738,398 | 5,164,708 | 1,317 | 1984 to present | ARPAV |
| B1a[a] | 749,617 | 5,149,008 | 2,150 | Sept 2013 to present | LPSB |
| B1b[a] | 749,617 | 5,149,008 | 2,150 | Sept 2013 to present | LPSB |
| B2[a] | 749,275 | 5,148,313 | 1,666 | Jul 2014 to present | UNI |
| B3 | 749,685 | 5,149,063 | 1,760 | Aug 2013 to Oct 2013 | ARPAV |
| B4 | 749,094 | 5,147,733 | 1,335 | 1984 to present | ARPAV |
| B5 | 746,273 | 5,148,299 | 968 | 1996 to present | ARPAV |
| SA1 | 745,500 | 5,161,912 | 2,241 | Jul 2009 to present | UNI |
| SA2 | 744,016 | 5,155,350 | 1,519 | 2016 to present | UNI |
| SA3 | 743,501 | 5,157,552 | 2,240 | 1992 to present | ARPAV |
| SA4 | 749,027 | 5,163,227 | 1743 | 1992 to present | ARPAV |
| SA5[a] | 739,803 | 5,158,433 | 1,270 | 1984 to present | ARPAV |

*Note*. Coordinates shown are UTM zone 32°N; A, B, and SA are the abbreviations for rain gauges that correspond to the Fiames network, the Rovina di Cancia one, and the stand alone rain gauges, respectively. The acronyms UNI, ARPAV, and LPSB refer to the universities of Bologna and Padova, the Regional Agency for Environmental Prevention and Protection of Veneto, and the Land Protection Service of the Province of Belluno. Rain gauges B1a and B1b are placed at 1 m distance each other and are referred as B1 in other tables and figures.

[a]Used by Gregoretti et al. (2016).

### 2.2. Monitoring Networks and Rainfall Data

Rainfall data used in this work derives from two sources, that is, rain gauges and a C-band Doppler weather radar. Since 2009, rain gauges were positioned in the headwater basins to cover as much as possible this area, also considering the existing ones of the public authorities. Therefore, two rainfall monitoring networks have been implemented in a high-mountain environment. The two monitoring networks are those in the Fiames area (Cortina d'Ampezzo; Figure 1c) and in the Rovina di Cancia basin (Borca di Cadore; Figure 1d) far from each other about 15 km. The networks consist of 10 tipping bucket rain gauges in the area of Fiames (A rain gauges) and 6 in the area of Rovina di Cancia (B rain gauges). In both areas, rain gauges are positioned both upstream and downstream the initiation areas of DFs. Two other single rain gauges were installed close to the initiation area of Rio Gere (SA1) and Punta Nera (SA2) DFs (Cortina d'Ampezzo). Furthermore, we use data recorded by other three rain gauges (SA3, SA4, and SA5) of ARPAV, placed in the Boite river valley. Rain gauges sample precipitation at 5-min intervals. All the rain gauges and their related monitoring networks are listed in Table 2: 2 are managed by LPSB, 6 by ARPAV, 13 by the Universities of Bologna and Padova. Those about the two universities are mounted on some monitoring stations (Bernard, Berti et al., 2019; Bernard et al., 2020; Berti et al., 2020; Simoni et al., 2020) or are independent rain gauges. Their maintenance is quite tiring because they are scattered and at different altitudes, near initiation areas or higher. Moreover, due to the difficult environmental conditions, some gauges were temporarily subjected to malfunction and data missed. The use of alternative sensors to overcome such drawback, as disdrometers (Fehlmann et al., 2020), has been evaluated and planned for next monitoring seasons. In Table 3, for each

**Table 3**
*Summary of Debris-Flow Events With the Triggering Rainfall Since 2009*

| Event | Watershed | Reference rain gauge | Distance RG-centroid (km) | Rainfall depth (mm) | Duration (min) | Max rainfall intensity (mm/5 min) | Operative Rain gauge N | Time of occurrence hh:mm GMT |
|---|---|---|---|---|---|---|---|---|
| 18/07/2009[a] | Rovina di Cancia | B4 | 1.3 | 46.4 | 150 | 11.6 | 7 | 03:40 |
| 22/08/2009 | Rudavoi | SA1 | 0.6 | 18.2 | 30 | 7.4 | 7 | – |
| 04/07/2011[a] | Fiames 1 | A1 | 0.8 | 13.4 | 35 | 2.5 | | 21:46 |
| | Fiames 2 | A10 | 1.5 | 28.2 | 75 | 3.8 | 7 | – |
| 18/08/2011[a] | Fiames 1 | A1 | 0.6 | 23.4 | 40 | 10.5 | | 18:05 |
| | Fiames 2 | A10 | 1.5 | 30.6 | 35 | 7.6 | 8 | – |
| 26/07/2013[a] | Rovina di Cancia | B5 | 3.3 | 21.6 | 70 | 3.2 | 15 | – |
| 19/08/2013[a] | Rovina di Cancia | B3 | 0.6 | 29.6 | 50 | 7.8 | 15 | – |
| 07/06/2015 | Fiames 1 | A3 | 0.3 | 15.2 | 30 | 5.8 | 15 | 22:18 |
| 23/06/2015 | Punta Nera | SA3 | 1.8 | 9.0 | 80 | 1.2 | 16 | – |
| 08/07/2015 | Punta Nera | SA3 | 1.8 | 15.4 | 85 | 4.4 | 19 | – |
| 17/07/2015 | Rio Gere | SA1 | 0.7 | 19.5 | 40 | 9.5 | 17 | – |
| 23/07/2015[b] | Rovina di Cancia | B1 | 0.1 | 38.1 | 40 | 8.2 | 20 | 14:05 |
| 25/07/2015[c] | Fiames 1 | A6 | 0.2 | 18.4 | 30 | 5.8 | 16 | – |
| 04/08/2015[b] | Rovina di Cancia | B1 | 0.8 | 39.2 | 40 | 9.9 | 17 | 18:37 |
| | Rio Rudan | B1 | 1.2 | 39.2 | 40 | 9.9 | | – |
| | Ru Secco | B1 | 2.4 | 39.2 | 40 | 9.9 | | – |
| 08/08/2015 | Punta Nera | SA3 | 1.8 | 19.2 | 85 | 6.2 | 13 | – |
| 16/06/2016 | Punta Nera | SA3 | 1.8 | 4.8 | 35 | 1.6 | 17 | – |
| 24/06/2016 | Punta Nera | SA2 | 0.8 | 6.0 | 35 | 1.5 | 18 | – |
| 27/06/2016 | Punta Nera | SA2 | 0.8 | 6.0 | 70 | 1.0 | 18 | – |
| 13/07/2016 | Punta Nera | SA2 | 0.8 | 5.5 | 30 | 1.5 | 18 | – |
| 21/07/2016[d] | Punta Nera | SA2 | 0.8 | 8.4 | 25 | 4.0 | 19 | 18:32 |
| 05/08/2016[d] | Punta Nera | SA2 | 0.8 | 14.4 | 155 | 1.4 | 19 | 09:14 |
| 14/08/2016[d] | Punta Nera | SA2 | 0.8 | 4.4 | 15 | 3.2 | 20 | 19:03 |
| 18/08/2016[d] | Punta Nera | SA2 | 0.8 | 7.4 | 35 | 3.2 | 20 | 17:10 |
| 20/08/2016[d] | Punta Nera | SA2 | 0.8 | 25.6 | 325 | 1.6 | 20 | – |
| 21/08/2016[d] | Punta Nera | SA2 | 0.8 | 5.8 | 25 | 3.4 | 20 | 15:13 |
| 04/09/2016[d] | Punta Nera | SA2 | 0.8 | 21.4 | 155 | 4.8 | 20 | 18:02 |
| 22/06/2017[d] | Punta Nera | SA2 | 0.8 | 20.8 | 45 | 7.6 | 13 | 19:45 |
| 02/08/2017[d] | Punta Nera | SA2 | 0.8 | 14.6 | 20 | 6.8 | 15 | 14:58 |
| 04/08/2017[d] | Punta Nera | SA2 | 0.8 | 19.8 | 75 | 6.2 | 16 | 23:42 |
| | Rio Gere | SA1 | 0.7 | 46.5 | 80 | 8.5 | | – |
| 12/09/2017 | Punta Nera | SA2 | 0.8 | 37.8 | 410 | 1.4 | 15 | – |
| 05/07/2018[b] | Rovina di Cancia | B1 | 0.1 | 36.9 | 110 | 7.1 | 12 | 16:45 |
| 14/07/2018[d] | Punta Nera | SA2 | 0.8 | 15.4 | 25 | 9.6 | 13 | 21:13 |
| 01/08/2018[b] | Rovina di Cancia | B1 | 0.1 | 50.0 | 175 | 11.0 | 13 | 20:58 |
| 09/08/2018[d] | Punta Nera | SA2 | 0.8 | 16.6 | 35 | 6.8 | 13 | 12:02 |
| 01/07/2020[b] | Rovina di Cancia | B1 | 0.1 | 27.0 | 60 | 14.0 | 13 | 13:10 |

**Table 3**
*Continued*

| Event | Watershed | Reference rain gauge | Distance RG-centroid (km) | Rainfall depth (mm) | Duration (min) | Max rainfall intensity (mm/5 min) | Operative Rain gauge N | Time of occurrence hh:mm GMT |
|---|---|---|---|---|---|---|---|---|
| 23/07/2020 | Rio Gere | SA1 | 0.7 | 8.4 | 30 | 4.4 | 15 | – |
| 29/08/2020[b] | Rovina di Cancia | B1 | 0.1 | 31.9 | 140 | 3.7 | 13 | 14:30 |

*Note*. For each event, we report the hit watershed, the reference rain gauge, its distance to the basin centroid, the features of the recorded precipitation and the time of DF triggering, when observed. We also report the number of operative rain gauges at that time.
[a]Degetto et al. (2015). [b]Simoni et al. (2020). [c]Berti et al. (2020). [d]Bernard, Berti et al. (2019).

DF event, we report the features of the DF triggering precipitation, recorded by the operating rain gauge nearest to the basin centroid. The triggering rainfall is the rainfall depth fallen from the beginning of precipitation to the time of DF occurrence (Gregoretti & Dalla Fontana, 2008). For identifying the rainfall beginning time, we applied the definition of burst used by Coe et al. (2008). The timing of occurrence is known by the monitoring stations of Bernard, Berti et al. (2019); Berti et al. (2020); Simoni et al. (2020) for 20 of the 41 DFs (Table 3). Therefore, for the sake of homogeneity, we used the entire precipitation of the event in all the cases. In Supporting Information Material, we show that the outcomes for the 23 events in which DF timing is known, do not change excessively when considering the "real" triggering rainfalls.

The weather radar is located on the top of Mount Macaion at 1860 m a.s.l. (Bolzano province), about 70 km far from the study area (Figure 1). Technical information about the instrumentation is reported in Marra et al. (2014). This radar is not the same used by Orlandini and Morlini (2000) for their study in this area. Precipitations are estimated from the observations of radar reflectivity, with a high resolution both in time (5 min) and in space ($0.5 \times 0.5$ km$^2$). More in detail, data furnished by the radar-managing institution and used in this study concern the intensities corresponding to the maximum reflectivity observed along the vertical of each pixel. The conversion from reflectivity to rainfall intensity is carried out using the $Z$-$R$ relationship of Marshall-Palmer (Marshall & Palmer, 1948). This relation is used by the managing institution as the standard one, independently from the type of precipitation. In the upper left panel of Figure 1, it is possible to see the degree of occlusion of the radar beam, shown as minimum elevation above the terrain level visible by the radar beam. The rain gauge network A and the rain gauges SA1, SA2 and, SA3 seem affected by limited problems of occlusion, whereas the radar beam cannot cover at least 500 m or more of the vertical profile above the other rain gauges. However, no other corrections are applied to the rainfall estimates.

## 3. Methods

The objective of this research is to evaluate the ability of a hydrological model to predict the occurrences of DFs by using different rainfall estimates. At first, we compare the Mt. Macaion radar estimated precipitations with the corresponding ground data measurements to evaluate the employing of the radar technology to headwater basin hydrology for determining the DF triggering conditions for early warning purposes. The comparison is initially carried out between the punctual measurements and the corresponding pixel estimates of radar by using statistical indexes. The radar-rainfall estimates are then corrected following two different approaches and the comparison is carried out on the basin mean areal rainfall. Finally, we evaluate the potential use of the extracted Scenarios (raw and corrected radar-rainfall estimates) to model DF triggering runoff and comparing the results with those provided by using the rain gauge data.

### 3.1. Statistics for Comparing Ground Data of Rainfall with Those Estimated by Radar

To evaluate differences between radar and rain gauge rainfalls, several statistics are considered. Ground data are selected as the independent variable (direct measurement of rainfall depths), whereas radar-rainfall values are chosen as the auxiliary one (rainfall depths estimated from reflectivity) according to Skinner et al. (2009). To evaluate the relationship between rainfall quantities, we calculate the following indexes commonly used for this task (Cunha et al., 2013; Vogl et al., 2012):

- the normalized bias (NB), a measure of the overall deviation of radar values compared to the corresponding rain gauge measurements, whose optimal value is 0:

$$NB = 100\frac{\sum(R_{i,t} - G_{i,t})}{\sum G_{i,t}} \tag{1}$$

- the root mean square error (RMSE) that represents the dispersion of radar estimates with a best possible value of 0:

$$RMSE = \sqrt{\frac{\sum(R_{i,t} - G_{i,t})^2}{N}} \tag{2}$$

- the correlation coefficient (corr) that indicates the linear correlation between the two data sets, varying between −1 and 1:

$$corr = \frac{cov[R,G]}{\sigma_R \sigma_G} \tag{3}$$

- the Nash-Sutcliffe efficiency coefficient (EC), a score proportional to the variance of quantities, varying between $-\infty$ and 1:

$$EC = 1 - \frac{\sum(R_{i,t} - G_{i,t})^2}{\sum(G_{i,t} - \overline{G_t})^2} \tag{4}$$

The quantities $R_{i,t}$ and $G_{i,t}$ indicates the rainfall depths estimated/recorded by the radar/rain gauges at the $i$th position at the time $t$, $\overline{G_t}$ denotes the rain gauge average in space, $N$ is the number of compared measure pairs, $cov$ represents the covariance operator, and $\sigma_X$ the standard deviation of the variable $X$. These indexes are separately computed on the whole area for each rainfall event, considering all the rain gauges working at the same time. To limit the influence on the scores of low rain rates, we only consider the time steps for which the values of rain intensity of either the rain gauges or the radar is greater than the resolution of the tipping bucket rain gauge, that is, 2.4 mm/h.

### 3.2. Bias Correction Methods

To give more consistency to radar data, we applied some correction methods. First, we implemented another equation to make the conversion from reflectivity to rainfall intensity, the relationship $Z$-$R$ of NEXRAD, more suitable for accounting for convective events (Anagnostou et al., 2010; Fulton et al., 1998). As reported in Section 1, in a mountain environment the choice of the best method to combine rain gauge and radar data is fundamental. In the past, several interpolation methods have been proposed, considering data provided by rain gauges as truth and those by radar as auxiliary information. Erdin (2009) categorized all the methods into three main classes. The first one includes the adjustment of radar images to rain gauge measures. This class includes those methods which modify characteristics of radar data to match as well as possible the measurement given by the rain gauges (Gjertsen et al., 2004). Hence, these methods are useful to improve the accuracy of radar-rainfall fields and are often used to post-process radar measurements (Germann et al., 2006). However, it is important to evaluate uncertainties in rain gauge measurements before developing a $Z$-$R$ relation that considers those rain gauges as ground truth (Hasan et al., 2014), otherwise, these uncertainties will affect the results of hydrological modeling (Habib et al., 2008). The second class includes the disaggregation of rain gauge fields using radar information. These methods can be used to fill the gaps of rain gauges through the spatial pattern provided by radar (DeGaetano & Wilks, 2009) or to achieve a higher resolution in time (Wüest et al., 2010). The third class embraces all the geostatistical approaches. Based on the theory of regionalized variables, geostatistics allows predicting values of an analyzed variable at unsampled locations evaluating the spatial correlation between its neighboring measurements (Goovaerts, 1997, 1999). There are several options for modeling spatial dependencies of precipitation data, that is, the choice of semivariogram

(Holawe & Dutter, 1999), and likewise combination methods, as co-kriging (Creutin et al., 1988; Krajewski, 1987), kriging with external drift (KED; Ahmed & De Marsily, 1987; Verworn & Haberlandt, 2011), co-KED (Sideris et al., 2014), or conditional merging (Ehret, 2003; Sinclair & Pegram, 2005).

In this work, two different approaches for improving estimates of rainfall fields are selected and compared, both carried out on a 5-min scale. The former consists in the adjustment of radar data to the measures of a reference rain gauge hereinafter called corrected radar, the latter is the KED approach.

#### 3.2.1. The Corrected Radar Approach

The corrected radar approach is carried out to maintain the locally recorded variability of radar rainfall fields. The method eliminates the difference between the rainfalls recorded by the reference rain gauge and the corresponding radar pixel for each time step. The radar rainfall estimates for every pixel are rescaled by shifting radar fields to fill the gap between reference gauge measurements and the corresponding pixel radar-rainfall estimates. The bias adjustment is additive following the example of Borga (2002). He evaluated a mean-field bias between radar and rain gauge rainfalls on the entire study area. In our case, the rescaling of the precipitation field is carried out considering the single rain gauge nearest to the basin centroid without any other topographic considerations.

#### 3.2.2. The KED Approach

The KED approach has been chosen because it permits the estimation of a nonstationary random function considering the spatial dependence of a primary variable and one or more auxiliary variables, linearly related to the primary one. The choice has been supported by the results of various studies (many of which reported in Ly et al., 2013) that highlight that KED estimates tend to be more accurate, especially when weather radar maps are used as external drift. Hence, it is assumed that the expected value of the main variable $Z(\boldsymbol{x})$ is linearly related to $n$ additional drift variables $Y_k(\boldsymbol{x})$ through the unknown coefficients $b_k$:

$$E\left[Z(\boldsymbol{x}) \mid Y_k(\boldsymbol{x})\right] = b_0 + \sum_{k=1}^{n} b_k Y_k(\boldsymbol{x}) \tag{5}$$

A second basic hypothesis affirms that the variance of the increment of $Z(\boldsymbol{x})$ between two points simply depends on its distance vector $\boldsymbol{h}$:

$$Var\left[Z(\boldsymbol{x}+\boldsymbol{h}) - Z(\boldsymbol{x})\right] = E\left\{\left[Z(\boldsymbol{x}+\boldsymbol{h}) - Z(\boldsymbol{x})\right]^2\right\} = 2\gamma(\boldsymbol{h}) \quad \boldsymbol{x} \in D \tag{6}$$

where $\gamma(\boldsymbol{h})$ is the semivariogram. The KED estimator for an unknown point $\boldsymbol{x}_0$ consists of a weighted sum of the $p$ surrounding observation $Z(\boldsymbol{x}_i)$:

$$Z(\boldsymbol{x}_0) = \sum_{i=1}^{p} \lambda_i Z(\boldsymbol{x}_i) \tag{7}$$

where the $\lambda_i$ weights have to be estimated by the kriging system:

$$\begin{gathered} \sum_{j=1}^{p} \lambda_j \gamma(\boldsymbol{x}_i - \boldsymbol{x}_j) + \mu_0 + \sum_{k=1}^{n} \mu_k Y_k(\boldsymbol{x}_i) = \gamma(\boldsymbol{x}_i - \boldsymbol{x}_0) \quad i = 1,\ldots,p \\ \sum_{j=1}^{p} \lambda_j = 1 \\ \sum_{j=1}^{p} \lambda_j Y_k(\boldsymbol{x}_j) = Y(\boldsymbol{x}_0) \quad k = 1,\ldots,n \end{gathered} \tag{8}$$

where $\mu_k$ are Lagrange multipliers, whereas the $b_k$ coefficients of Equation 5 are implicitly estimated, with the hypothesis that the additional variables $Y_k$ are known at all points $\boldsymbol{x}$.

In this work, the KED approach estimates the rainfall field using the precipitations recorded by rain gauges as the primary variable, and radar rainfall field as an auxiliary one. Generally, also the orography of a region influences precipitations, mainly if it is complex. If rainfall and elevation are strongly correlated, a map of

**Table 4**
*Calibrated Parameters of the Hydrological Model*

| Parameter | |
|---|---|
| CN | |
| *Rocks* | 91.3 |
| *Scree* | 65 |
| *Bushes* | 61 |
| $U_S$ (m/s) | |
| *Rocks* | 0.7 |
| *Other terrains* | 0.1 |
| $K_S$ ($m^{1/3}/s$) | 9 |
| $f_c$ (cm/h) | |
| *Rocks* | 3.12–0.15*P* |
| *Scree* | 10.5 |
| *Bushes* | 6.5 |

*Note*. The relation for evaluating the Hortonian infiltration $f_c$ is effective only for AMC I events. *P* denotes the cumulated precipitation fallen in the 2 days preceding the event (expressed in mm).

topography could be used to improve the performance of interpolation (Masson & Frei, 2014). The relationship between rainfall and elevation is evaluated for each considered event following Nikolopoulos et al. (2015). The rain gauges are grouped according to 200-m elevation intervals and for each interval, both the maximum intensity and the mean of cumulative depths are computed. Such quantities show a non-monotonic behavior so that elevation and rainfall result uncorrelated. Therefore, the elevation is not used as an auxiliary variable.

To evaluate the spatial dependence of rainfall, the semivariogram estimation should be carried out for each time step. It would be time-consuming: for each time step, we need to evaluate a specific experimental semivariogram and, then, the relative theoretical model that fits it. To simplify this procedure, we follow the approach used by Haberlandt (2007). We estimate the experimental semivariogram $\overline{\gamma}^*(\boldsymbol{h})$ as average on time of the several interval-specific semivariograms:

$$\overline{\gamma}^*(\boldsymbol{h}) = \frac{1}{2n}\sum_{t=1}^{n}\frac{1}{n_t(\boldsymbol{h})s_t^2(Z)}\sum_{i=1}^{n_t(\boldsymbol{h})}[Z(\boldsymbol{x}_i+\boldsymbol{h},t)-Z(\boldsymbol{x}_i,t)]^2 \quad (9)$$

where $n$ and $n_t(\boldsymbol{h})$ are respectively the number of time steps $t$ and couples of data separated by the distance $\boldsymbol{h}$, and $Z(x_i,t)$ is the value assumed by the rain gauge precipitation in the location $x_i$ at time step $t$. For each time step, the specific experimental semivariogram is standardized by the variance $s_t^2$. To ensure that the semivariogram is continuous and evaluable for every distance $\boldsymbol{h}$, a theoretical model $\gamma(\boldsymbol{h})$ is fit on the values provided by the experimental semivariogram $\overline{\gamma}^*(\boldsymbol{h})$. As a theoretical semivariogram, we use a combination of the spherical model and a nugget effect. Moreover, we further simplify this approach, using an "average" theoretical semivariogram: its parameters are evaluated as the median of the parameters of every event semivariogram. We choose the median value because it is less sensitive to outliers than the mean value (Höhle & Höhle, 2009). The median semivariogram will be used in two different interpolations: (1) considering the entire rain gauge data set; (2) considering the rain gauges of the regional monitoring network, managed by ARPAV (Table 2), to point out the relevance of maintaining a high-elevation rain-gauge network in a mountain area.

When the KED method is applied for merging rain gauge and radar data collected at a high temporal resolution, numerical instabilities could appear solving the kriging system (Equation 8). This considerable problem might occur when the variation of the modeled variable is not smooth in space, for example, when many rain gauges record zero precipitation. If the kriging system turns out to be singular or ill-conditioned, the theoretical semivariogram would be manually adapted, that is, the parameters of the theoretical semivariogram would be manually varied to best fit the points of the experimental semivariogram.

### 3.3. The Hydrological Model for Headwater Rocky Basins

Runoff modeling is essential for the determination of debris-flow occurrence that takes place when runoff exceeds a critical discharge (Gregoretti & Dalla Fontana, 2008). Therefore, we used an event-based distributed hydrological model designed for a headwater rocky environment that has been satisfactorily calibrated and tested against field observations (Gregoretti et al., 2016). Excess rainfall is computed for each pixel by a simplified Hortonian law when the rainfall intensity is larger than the infiltration rate $f_c$, or by the Curve Number method of Soil Conservation Service, when the rainfall intensity is smaller than the infiltration rate $f_c$. The first mechanism simulates the contribution to runoff of excess rainfall whereas the second one simulates the contribution of interflow. Runoff is transferred to the drainage channel network along the steepest slope direction, with slope velocities that are constant but different for each land use. Finally, it is routed to the watershed outlet using the matched diffusivity kinematic model of Orlandini and Rosso (1996). Pa-

rameters of the model are the curve number CN, the infiltration rate $f_c$, the slope velocity $U$, and the Gaucker-Strickler coefficient $K_S$ (Table 4).

In Gregoretti et al. (2016), the hydrological model was calibrated by comparing the simulated discharges with those measured at the outlet of the rocky channel of Fiames 1. Rainfall fields used as input of the model were recorded by using two rain gauges placed just upstream and downstream of the watershed. In particular, the values of the parameters are constant for all simulations but the infiltration rate that depends on the 2-days previous rainfall depth. The model has been also tested, according to Rengers et al. (2016), through the timings of the initiation of four DF events occurred in the Acquabona and Rovina di Cancia basins. The calibration of parameters has been carried out only for rocky terrains (according to the Coordination of Information on the Environment land cover map published in 2012) because the headwater basin of Fiames 1 is almost exclusively composed of this kind of soil. In presence of scree, bushes or dwarf mountain pines, the values of parameters concerning CN, slope velocity and infiltration rate are those provided by Gregoretti et al. (2016).

### 3.4. Scenarios for Hydrological Modeling

Rainfall is the most important input for hydrological modeling; therefore, understanding how rainfall errors condition hydrological applications, quantifying uncertainties on the results of models has great importance (Chen et al., 2013). Hydrological modeling was carried out by using different scenarios, outcomes of correction methods shown in Section 3.2. We applied different scenarios to find the easier and robust method to adjust radar estimates for the purpose of improving the modeling results. The rainfall field scenarios used as input of modeling are:

1. The nearest neighbor interpolation of rain gauges data;
2. The raw radar estimates furnished by the radar managing institution;
3. The radar estimates transformed by using the NEXRAD equation (Fulton et al., 1998);
4. The corrected radar fields, i.e., the correction of radar maps by means of a reference rain gauge;
5. The KED interpolation;
6. The KED interpolation with the "median" semivariogram;
7. The KED interpolation with the "median" semivariogram of the rain gauges belonging to the ARPAV network, that is, those not explicitly used in DF monitoring.

For each modeled event, the peak value of the simulated runoff is then compared with a triggering discharge: DF initiates when runoff discharge becomes larger than the threshold value. Such approach initially used in sediment transport for determining the incipient motion condition (Bathurst et al., 1987) has been extended to DF initiation by Tognacca et al. (2000), and nowadays, it is widely used for determining the triggering conditions of DFs (Berti et al., 2020; Gong et al., 2020; McGuire & Youberg, 2020; Pastorello et al., 2020; Raymond et al., 2020; Tang et al., 2019; Wei et al., 2018) rather than the rainfall-intensity thresholds.

The critical discharge equation for DF triggering here used is that proposed by Gregoretti and Dalla Fontana (2008), tested on about 30 occurred DFs:

$$Q_{CRIT} = B\,0.78\frac{d_M^{1.5}}{\tan\theta_{TRIG}^{1.27}} \tag{10}$$

where $B$, $d_M$, and $\theta_{TRIG}$ are, respectively, the bottom width, the mean size of debris, and the bed slope angle at the triggering section.

## 4. Results and Discussion

### 4.1. Comparison Between Measured and Estimated Rainfalls

In Figure 2, we show, for each DF event listed in Table 3, the values of the computed statistics introduced in Subsection 3.1, that quantify the differences between gauged and radar-estimated rainfalls. Statistics were computed using all the active rain gauges on the entire study area.

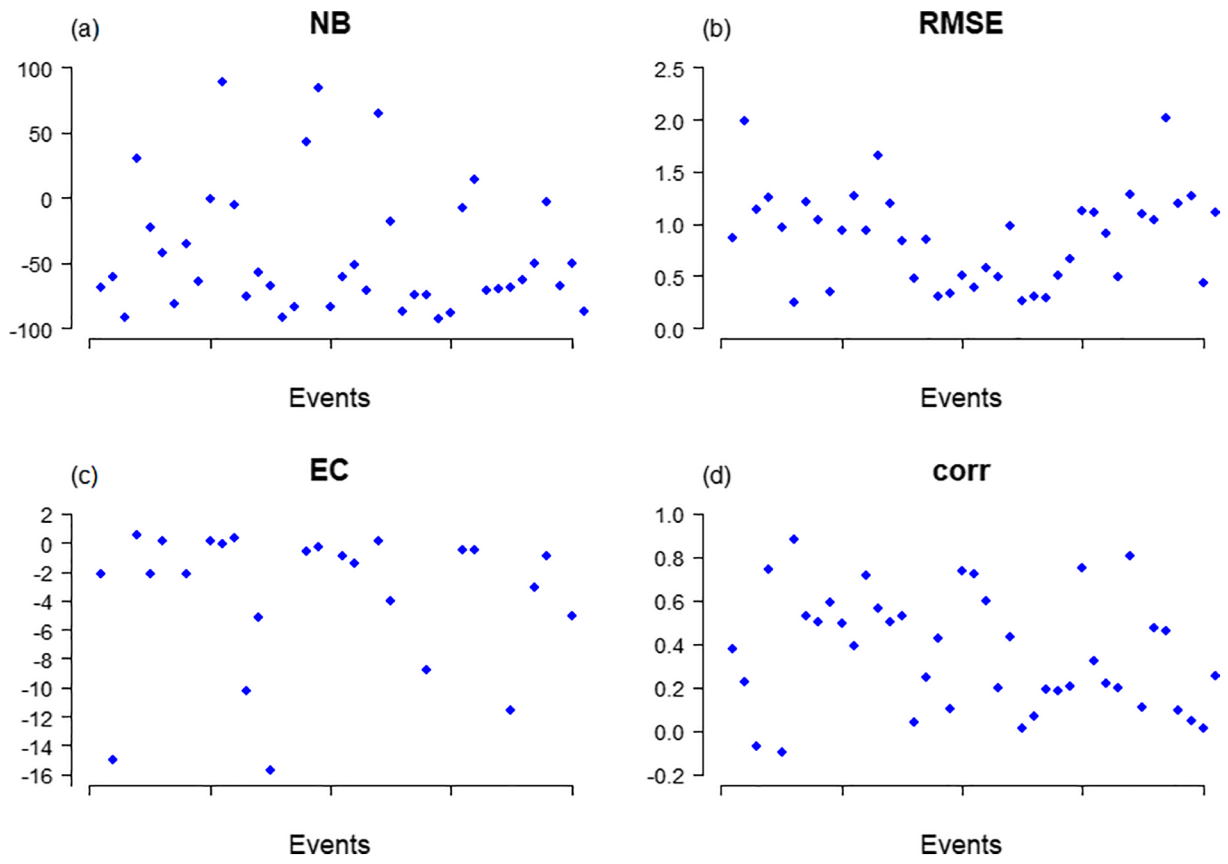


**Figure 2.** Statistical indexes for the comparison between radar and rain gauge rainfall elds computed for each analyzed event. Panel (a) refer to normalized bias (NB), (b) refers to the root mean square error (RMSE), (c) refers to the Nash-Sutcliffe efficiency index (EC), and (d) refers to the correlation coefficient (corr). For graphical purposes, the lower boundary of panel (c) is limited to −16.0.

The NB, RMSE, and EC indexes demonstrate the relevant difference between the radar and rain gauge rainfall fields. The NB percentages (Figure 2a) range between −93.5% and 89.1%, with a mean value of −41.2% (most of the events are definitely below zero). If the NB index describes a systemic underestimation trend, RMSE quantifies the random error between observed rainfalls (Neary et al., 2004): the greater the index, the greater the existing random gaps between corresponding pairs. In this case (Figure 2b), RMSE has an average value of 0.9, varying between 0.2 and 2.0. Finally, the EC index (Figure 2c) varies inside a wide range (from −901.4 to 0.5), showing the unpredictable behavior of raw radar estimates in comparison with the rain gauge measures, in accordance to Verworn and Haberlandt (2011). These outcomes are expected because of the multiplicity of problems in mountainous areas (Andrieu et al., 1997). On the other hand, considering the small sampling precipitation interval (5 minutes), values of correlation show good spatio-temporal accordance between the radar and the rain gauge fields for most of the events (it ranges between −0.1 and 0.9 with a mean value of 0.4). Differently from the other indexes, the correlation does not consider the disagreement between measured rainfall fields but enables to compare the meteorological structure of the recorded precipitations. It is evident that other studies (e.g., Cunha et al., 2013; Goovaerts, 2000; Velasco-Forero et al., 2009) obtained higher correlation values but in less complex topographies and using larger time intervals for comparing precipitations.

### 4.2. Bias Correction

Once the bias between recorded rainfalls has been assessed, raw radar data are corrected according to the methodologies pointed out in Section 3.2. The improvements on radar data are evaluated comparing for each event the mean areal precipitation fallen in the basin delimited to its DF initiation area. The reason for changing the scale, from the 300 $km^2$ study area used for the previous point-comparison to the watershed

Water Resources Research

10.1029/2020WR027893

**Table 5**
*Mean Areal Rainfall Depth ($R_M$) and Peak of Simulated Discharge (Q) for Each Scenario and Event (the Terms in Brackets Refer to the Percentage Differences From Corresponding Values of Scenario 1)*

| | | Scenario 1 | | Scenario 2 | | Scenario 3 | | Scenario 4 | | Scenario 5 | | Scenario 6 | | Scenario 7 | |
|---|---|---|---|---|---|---|---|---|---|---|---|---|---|---|---|
| Event | Watershed | $R_M$ (mm) | $Q$ ($m^3/s$) | $R_M$ (mm) | $Q$ ($m^3/s$) | $R_M$ (mm) | $Q$ ($m^3/s$) | $R_M$ (mm) | $Q$ ($m^3/s$) | $R_M$ (mm) | $Q$ ($m^3/s$) | $R_M$ (mm) | $Q$ ($m^3/s$) | $R_M$ (mm) | $Q$ ($m^3/s$) |
| 18-07-09 | Rovina di Cancia | 46.4 | **5.4** | 19.1 (−59%) | **1.7** (−68%) | 20.2 (−57%) | **2.2** (−59%) | 37.3 (−20%) | **4.5** (−17%) | 35.4 (−24%) | **2.9** (−46%) | 34.5 (−26%) | **2.8** (−48%) | 35.8 (−23%) | **2.8** (−48%) |
| 22-08-09 | RioGere | 18.2 | **1.0** | 5.9 (−67%) | 0.0 (−100%) | 5.9 (−68%) | 0.0 (−100%) | 21.6 (19%) | **1.4** (45%) | 29.5 (62%) | **3.3** (240%) | 23.9 (32%) | **1.9** (95%) | 24.3 (34%) | **1.9** (97%) |
| 04-07-11 | Fiames 1 | 21.6 | **0.3** | 10.5 (−51%) | 0.0 (−93%) | 10.6 (−51%) | 0.0 (−93%) | 27.9 (29%) | **0.3** (3%) | 25.0 (16%) | **0.4** (31%) | 25.3 (17%) | **0.4** (40%) | 18.1 (−16%) | 0.1 (−65%) |
| | Fiames 2 | 28.2 | **0.6** | 13.7 (−51%) | 0.2 (−68%) | 14.7 (−48%) | 0.3 (−52%) | 29.5 (5%) | **1.2** (88%) | 24.7 (−13%) | **0.6** (−6%) | 24.6 (−13%) | **0.6** (−6%) | 20.8 (−26%) | **0.4** (−31%) |
| 18-08-11 | Fiames 1 | 17.6 | **0.3** | 56.6 (221%) | **1.2** (393%) | 73.6 (318%) | **1.9** (536%) | 27.8 (58%) | **0.9** (249%) | 24.1 (37%) | **0.6** (155%) | 26.1 (49%) | **0.7** (175%) | 47.7 (171%) | **1.6** (536%) |
| | Fiames 2 | 30.6 | **2.5** | 39.2 (28%) | **2.6** (5%) | 48.2 (58%) | **4.0** (59%) | 38.9 (27%) | **3.7** (51%) | 22.6 (−26%) | **1.6** (−34%) | 22.5 (−26%) | **1.6** (−36%) | 43.2 (41%) | **5.3** (114%) |
| 26-07-13 | Rovina di Cancia | 21.6 | **1.1** | 2.4 (−89%) | 0.0 (−100%) | 1.8 (−92%) | 0.0 (−100%) | 13.3 (−39%) | 0.1 (−90%) | 4.5 (−79%) | 0.0 (−100%) | 4.1 (−81%) | 0.0 (−100%) | 4.1 (−81%) | 0.0 (−100%) |
| 19-08-13 | Rovina di Cancia | 30.4 | **3.8** | 1.9 (−94%) | 0.0 (−100%) | 1.5 (−95%) | 0.0 (−100%) | 30.4 (0%) | **3.5** (−9%) | 20.2 (−34%) | **3.3** (−14%) | 10.4 (−66%) | 0.2 (−94%) | 10.0 (−67%) | 0.2 (−95%) |
| 07-06-15 | Fiames 1 | 15.2 | **0.4** | 11.1 (−27%) | 0.1 (−72%) | 11.2 (−26%) | 0.1 (−74%) | 15.7 (3%) | **0.4** (−2%) | 15.8 (4%) | **0.4** (2%) | 15.9 (5%) | **0.4** (3%) | 9.2 (−40%) | **0.2** (−50%) |
| 23-06-15 | Punta Nera | 9 | 0.1 | 2.1 (−77%) | 0.0 (−100%) | 1.7 (−81%) | 0.0 (−100%) | 6.7 (−25%) | 0.1 (−39%) | 3.3 (−63%) | 0.0 (−100%) | 4.0 (−56%) | 0.0 (−94%) | 7.4 (−18%) | **0.2** (24%) |
| 08-07-15 | Punta Nera | 14 | **0.2** | 28.3 (102%) | **1.9** (703%) | 33.1 (226%) | **2.7** (1,245%) | 34.4 (145%) | **3.1** (1,212%) | 43.4 (210%) | **2.9** (1,103%) | 43.2 (208%) | **4.5** (1,781%) | 41.7 (198%) | **4.4** (1,740%) |
| 17-07-15 | Rio Gere | 19.5 | **1.3** | 30.5 (56%) | **8.5** (543%) | 36.6 (88%) | **13.7** (955%) | 21.6 (11%) | **1.4** (7%) | 17.1 (−12%) | **1.9** (39%) | 17.1 (−12%) | **1.9** (45%) | 21.0 (8%) | **1.9** (41%) |
| 23-07-15 | Rovina di Cancia | 36.9 | **5.8** | 20.4 (−45%) | **0.8** (−87%) | 23.2 (−37%) | **1.2** (−6%) | 38.8 (5%) | **4.4** (−24%) | 28.1 (−24%) | **3.1** (−47%) | 24.3 (−34%) | **2.4** (−59%) | 24.8 (−33%) | **2.6** (−56%) |
| 25-07-15 | Fiames 1 | 18.1 | **0.2** | 3.5 (−81%) | 0.0 (−100%) | 3.1 (−83%) | 0.0 (−100%) | 18.6 (2%) | **0.3** (33%) | 18.6 (2%) | **0.3** (24%) | 15.0 (−17%) | 0.1 (−37%) | 5.4 (−70%) | 0.0 (−100%) |
| 04-08-15 | Rovina di Cancia | 37.5 | **9.7** | 8.3 (−78%) | **0.9** (−90%) | 8.4 (−78%) | 0.1 (−99%) | 35.8 (−5%) | **8.5** (−13%) | 18.6 (−50%) | **4.9** (−50%) | 23.4 (−38%) | **3.6** (−63%) | 23.8 (−37%) | **3.9** (−60%) |
| | Rio Rudan | 39.2 | **13.4** | 8.4 (−78%) | **0.7** (−95%) | 8.5 (−78%) | **0.8** (−94%) | 34.8 (−11%) | **11.9** (−11%) | 30.2 (−23%) | **9.2** (−31%) | 33.0 (−16%) | **9.9** (−26%) | 33.9 (−13%) | **10.1** (−24%) |
| | Ru Secco | 42.2 | **7.8** | 14.5 (−66%) | 0.4 (-94%) | 15.1 (−64%) | **0.6** (−92%) | 44.2 (5%) | **8.8** (12%) | 36.9 (−12%) | **7.5** (−4%) | 39.2 (−7%) | **9.4** (20%) | 39.1 (−7%) | **9.0** (15%) |
| 08-08-15 | Punta Nera | 19.2 | **2.7** | 5.3 (−72%) | 0.0 (−98%) | 6.0 (−69%) | 0.1 (−98%) | 22.1 (15%) | **3.1** (17%) | 3.8 (−80%) | 0.0 (−100%) | 3.0 (−84%) | 0.0 (−100%) | 4.4 (−77%) | 0.0 (−99%) |
| 16-06-16 | Punta Nera | 4.8 | 0.0 | 1.0 (0%) | 0.0 (0%) | 0.7 (−85%) | 0.0 (0%) | 5.0 (0%) | 0.0 (0%) | 3.4 (0%) | 0.0 (0%) | 3.4 (−29%) | 0.0 (0%) | 3.4 (−29%) | 0.0 (0%) |

Water Resources Research

10.1029/2020WR027893

**Table 5**
*Continued*

| Event | Watershed | Scenario 1 | | Scenario 2 | | Scenario 3 | | Scenario 4 | | Scenario 5 | | Scenario 6 | | Scenario 7 | |
|---|---|---|---|---|---|---|---|---|---|---|---|---|---|---|---|
| | | $R_M$ (mm) | $Q$ ($m^3/s$) | $R_M$ (mm) | $Q$ ($m^3/s$) | $R_M$ (mm) | $Q$ ($m^3/s$) | $R_M$ (mm) | $Q$ ($m^3/s$) | $R_M$ (mm) | $Q$ ($m^3/s$) | $R_M$ (mm) | $Q$ ($m^3/s$) | $R_M$ (mm) | $Q$ ($m^3/s$) |
| 24-06-16 | Punta Nera | 6 | 0.0 | 2.6 (−57%) | 0.0 (−100%) | 1.7 (−71%) | 0.0 (0%) | 6.3 (6%) | 0.0 (−100%) | 4.5 (−24%) | 0.0 (−100%) | 4.6 (−24%) | 0.0 (−100%) | 2.2 (−64%) | 0.0 (−100%) |
| 27-06-16 | Punta Nera | 9 | **0.4** | 0.9 (−90%) | 0.0 (−100%) | 0.6 (−94%) | 0.0 (−100%) | 4.9 (−46%) | 0.1 (−88%) | 5.3 (−41%) | 0.1 (−81%) | 5.4 (−40%) | 0.1 (−83%) | 4.9 (−45%) | 0.1 (−84%) |
| 13-07-16 | Punta Nera | 18.5 | **2.3** | 12.5 (−33%) | **1.8** (−21%) | 13.2 (−29%) | **2.1** (−10%) | 19.8 (7%) | **2.8** (20%) | 20.5 (11%) | **3.5** (52%) | 19.6 (6%) | **3.6** (57%) | 35.2 (90%) | **11.6** (404%) |
| 21-07-16 | Punta Nera | 9 | 0.1 | 5.3 (−41%) | 0.0 (−100%) | 5.5 (−39%) | 0.0 (−100%) | 6.7 (−25%) | 0.0 (−99%) | 6.7 (−26%) | 0.0 (−100%) | 6.7 (−25%) | 0.0 (−100%) | 34.9 (288%) | **7.3** (10,625%) |
| 05-08-16 | Punta Nera | 12.2 | 0.1 | 2.6 (−79%) | 0.0 (−100%) | 1.7 (−86%) | 0.0 (−100%) | 14.4 (18%) | 0.1 (5%) | – (–) | – (–) | 10.6 (−13%) | 0.0 (−58%) | 8.8 (−28%) | 0.0 (−83%) |
| 14-08-16 | Punta Nera | 4.4 | 0.0 | 35.5 (706%) | **5.5** (5,453%) | 44.5 (912%) | **8.3** (8,230%) | 19.4 (342%) | **2.4** (23,770%) | 26.3 (497%) | **7.2** (72,360%) | 25.9 (488%) | **7.1** (70,800%) | 47.3 (976%) | **15.7** (156,640%) |
| 18-08-16 | Punta Nera | 7.4 | 0.0 | 2.3 (−70%) | 0.0 (−100%) | 2.0 (−73%) | 0.0 (−100%) | 2.7 (−63%) | 0.0 (−100%) | – (–) | – (–) | 10.1 (37%) | 0.2 (2043%) | 1.9 (−74%) | 0.0 (−100%) |
| 20-08-16 | Punta Nera | 20.6 | **1.2** | 1.0 (−95%) | 0.0 (−100%) | 0.6 (−97%) | 0.0 (−100%) | 20.7 (0%) | **1.2** (0%) | – (–) | – (–) | 11.0 (−47%) | **0.5** (−60%) | 9.4 (−54%) | **0.3** (−76%) |
| 21-08-16 | Punta Nera | 5.8 | **1.1** | 0.6 (−90%) | 0.0 (−100%) | 0.5 (−92%) | 0.0 (−100%) | 5.8 (0%) | **0.9** (−18%) | 7.4 (27%) | **1.7** (56%) | 6.5 (12%) | **1.3** (21%) | 1.6 (−72%) | 0.0 (−99%) |
| 04-09-16 | Punta Nera | 17.6 | **1.3** | 1.9 (−89%) | 0.0 (−100%) | 1.4 (−92%) | 0.0 (−100%) | 17.6 (0%) | **1.1** (−16%) | 15.3 (−13%) | 0.2 (−83%) | 10.1 (−43%) | 0.0 (−98%) | 10.0 (−43%) | 0.0 (−97%) |
| 22-06-17 | Punta Nera | 20.8 | **1.9** | 1.2 (−94%) | 0.0 (−100%) | 0.9 (−96%) | 0.0 (−100%) | 18.4 (−11%) | **1.9** (0%) | 16.3 (−22%) | **1.3** (−30%) | 16.1 (−22%) | **1.2** (−34%) | 17.5 (−16%) | **1.6** (−17%) |
| 02-08-17 | Punta Nera | 14.6 | **1.7** | 15.4 (6%) | **1.5** (−12%) | 17.4 (19%) | **2.2** (29%) | 20.5 (40%) | **1.7** (0%) | 20.2 (39%) | **1.7** (2%) | 20.2 (38%) | **1.7** (4%) | 8.2 (−44%) | **0.2** (−90%) |
| 04-08-17 | Punta Nera | 19.8 | **2.8** | 17.9 (−10%) | **0.9** (−69%) | 18.0 (−9%) | **1.3** (−54%) | 25.2 (27%) | **2.8** (0%) | 35.2 (78%) | **3.6** (286%) | 34.9 (76%) | **3.4** (237%) | 40.8 (106%) | **4.0** (43%) |
| | Rio Gere | 46.5 | **11.5** | 85.5 (84%) | **13.8** (20%) | 102.4 (120%) | **18.8** (63%) | 80.1 (72%) | **11.1** (−3%) | 105.5 (127%) | **19.7** (71%) | 144.3 (210%) | **23.6** (105%) | 149.4 (221%) | **24.5** (113%) |
| 12-09-17 | Punta Nera | 38 | **1.3** | 2.4 (−94%) | 0.0 (−99%) | 1.4 (−96%) | 0.0 (−100%) | 38.0 (0%) | **1.3** (0%) | – (–) | – (–) | 29.4 (−23%) | **0.7** (−49%) | 32.7 (−14%) | **0.7** (−42%) |
| 05-07-18 | Rovina di Cancia | 33.8 | **2.5** | 5.5 (−84%) | 0.0 (−100%) | 4.6 (−86%) | 0.0 (−100%) | 30.5 (−10%) | **1.7** (−32%) | 26.8 (−21%) | **1.0** (−58%) | 27.7 (−18%) | **1.2** (−53%) | 28.4 (−16%) | **1.3** (−48%) |
| 14-07-18 | Punta Nera | 15.4 | **1.1** | 3.3 (−78%) | 0.0 (−100%) | 3.0 (−81%) | 0.0 (−100%) | 15.1 (−2%) | **0.9** (−13%) | – (–) | – (–) | 12.9 (−16%) | **0.9** (−16%) | 1.3 (−92%) | 0.0 (−100%) |
| 01-08-18 | Rovina di Cancia | 34.5 | **3.4** | 11.8 (−66%) | 0.0 (−99%) | 11.7 (−66%) | 0.1 (−99%) | 32.7 (−5%) | **3.0** (−11%) | 28.1 (−19%) | **1.2** (−65%) | 30.4 (−12%) | **1.7** (−50%) | 32.4 (−6%) | **2.3** (−33%) |
| 09-08-18 | Punta Nera | 16.6 | **1.3** | 3.6 (−78%) | 0.0 (−100%) | 3.3 (−80%) | 0.0 (−100%) | 17.3 (4%) | **1.3** (−2%) | – (–) | – (–) | 17.4 (5%) | **1.3** (1%) | 15.2 (−8%) | **1.0** (−25%) |

**Table 5**
*Continued*

| Event | Watershed | Scenario 1 | | Scenario 2 | | Scenario 3 | | Scenario 4 | | Scenario 5 | | Scenario 6 | | Scenario 7 | |
|---|---|---|---|---|---|---|---|---|---|---|---|---|---|---|---|
| | | $R_M$ (mm) | $Q$ ($m^3$/s) | $R_M$ (mm) | $Q$ ($m^3$/s) | $R_M$ (mm) | $Q$ ($m^3$/s) | $R_M$ (mm) | $Q$ ($m^3$/s) | $R_M$ (mm) | $Q$ ($m^3$/s) | $R_M$ (mm) | $Q$ ($m^3$/s) | $R_M$ (mm) | $Q$ ($m^3$/s) |
| 01-07-20 | Rovina di Cancia | 24.7 | **3.5** | 3.4 (−86%) | 0.0 (−100%) | 3.4 (−86%) | 0.0 (−100%) | 25.5 (4%) | **3.3** (−6%) | 18.4 (−25%) | **1.4** (−60%) | 14.4 (−42%) | 0.6 (−83%) | 28.7 (16%) | **5.8** (66%) |
| 23-07-20 | Rio Gere | 8.4 | 0.0 | 1.4 (−83%) | 0.0 (0%) | 1.3 (−85%) | 0.0 (0%) | 7.5 (−11%) | 0.0 (0%) | 2.0 (−76%) | 0.0 (0%) | 2.0 (−76%) | 0.0 (0%) | 8.3 (−1%) | 0.0 (0%) |
| 29-08-20 | Rovina di Cancia | 35.4 | **2.1** | 4.0 (−89%) | 0.0 (−99%) | 3.3 (−85%) | 0.0 (−100%) | 31.3 (−12%) | **1.9** (−9%) | 26.0 (−27%) | **1.3** (−40%) | 24.2 (−32%) | **1.1** (−48%) | 25.1 (−29%) | **3.9** (90%) |

*Note.* In bold, the discharges larger than the basin debris-flow critical discharge.

extent, is for maintaining the observed variability of precipitation on the watersheds hit by the DF triggering storm. In such a case, methods for areal correction can be applied and their results compared. Table 5 and left inserts of Figure 3 summarize the differences between the raw and bias-corrected radar data. To avoid misunderstandings, we refer each rainfall field to the corresponding Scenario described in Section 3.4.

Scenario 1 (the nearest neighbor interpolation of rain gauge data) is chosen as a reference since it better describes reality, given the noticeable difference with the raw radar data reported in Section 4.1. The analysis of the percentage difference between the rainfall depths of each scenario and that of Scenario 1 is carried out for each event. Outliers are defined as values that fall outside the range $\left[Q_1 - 3(Q_3 - Q_1), Q_3 + 3(Q_3 - Q_1)\right]$, where $Q_1$ and $Q_3$ are the first and third quartiles (Tukey, 1977). These events are characterized by a high spatial variation of rainfall that the rain gauges cannot capture. Plotting the relative boxplots (Figure 3), the median of the percentage difference between the rainfall depths of Scenarios 1 and 2 or 3 (the raw radar estimates) is high: −73%. This means a noticeable underestimation of the rainfall field (the mean areal precipitation on DF basins). These outcomes mean that the used *Z-R* relation is not much significant. The Scenarios 4 (corrected radar field) and 5, 6, and 7 (KED interpolation with different degrees of averaging) are more similar to the ground-recorded rainfall field: 2%, −19%, −17%, and −18%, respectively (Figure 3a). A similar result could be deduced for the differences in maximum intensities (Figure 3b). Scenario 4 provides the best approximation to rainfalls of Scenario 1 (however, in Subsection 4.4, we will point out how the choice of the reference rain gauge for rescaling the rainfall fields is fundamental). The KED interpolation (Scenario 5) shows spreader differences than the corrected radar field (Scenario 4). A reason for this behavior has to be looked for: (1) the average of computed semivariograms; (2) the highly localized character of the triggering storms. A further demonstration is given by Scenarios 6 and 7: increasing the averaging of the semivariograms leads to a higher spreading of differences with respect to Scenario 1 as well as the use of a lower number of rain gauges in the interpolation. A different behavior can be inferred looking to the timings of maximum intensities (Figure 3c). In this case, the median values of differences are quite similar, ranging between 0% and 42%; the differences among scenarios lie in the interquartile range: the Scenarios 4–7 tend to overestimate the timing of maximum intensities respect to Scenario 1, whereas the timings of raw radar scenarios (2 and 3) are spread around the Scenario 1 timing, confirming the good correlation showed in Subsection 4.1.

### 4.3. Hydrological Modeling

We highlight now the results of hydrological modeling and prediction of DF triggering that are also reported in Table 5. For the simulations, we did not use the mean areal rainfalls but the distributed rainfall fields to better characterize the contribution to runoff of the rocky walls. In the case of Scenario 1, we subdivided each basin by using Thiessen polygons to identify the area of influence of rain gauges; for the remaining scenarios, each watershed has been subdivided considering the pixels of radar fields. A point needs to be clarified for Scenario 5: considering that the primary and the secondary variables must be linearly correlated for applying, simulations corresponding to Scenario 5 are carried out only when the correlation index is higher than 0.2, that is, in 35 events of the considered 41. For Scenarios 6 and 7, this is not necessary because of the made approximations. Results are shown in Figure 3d as the percentage difference between the simulated peak discharges provided by each Scenario and those corresponding to the reference scenario (Scenario 1). Boxplots show the marked underestimation of simulated peak discharges for Scenario 2 and 3 (raw radar data). Scenario 4 (corrected radar field) provides the best approximation for the simulated discharges with respect to Scenario 1 (the median of the percentage difference values is −2%), whereas the simulated peak discharges corresponding to KED scenarios are either close or in an intermediate position (−14%, −34%, and −33% the median difference values). The results of KED scenarios highlight that the worse the approximation in the interpolation, the greater the discrepancy in the outcomes. Results do not substantially differ from previous works on the use of radar data for the assessment of similar phenomena as flash floods. When hydrological models use

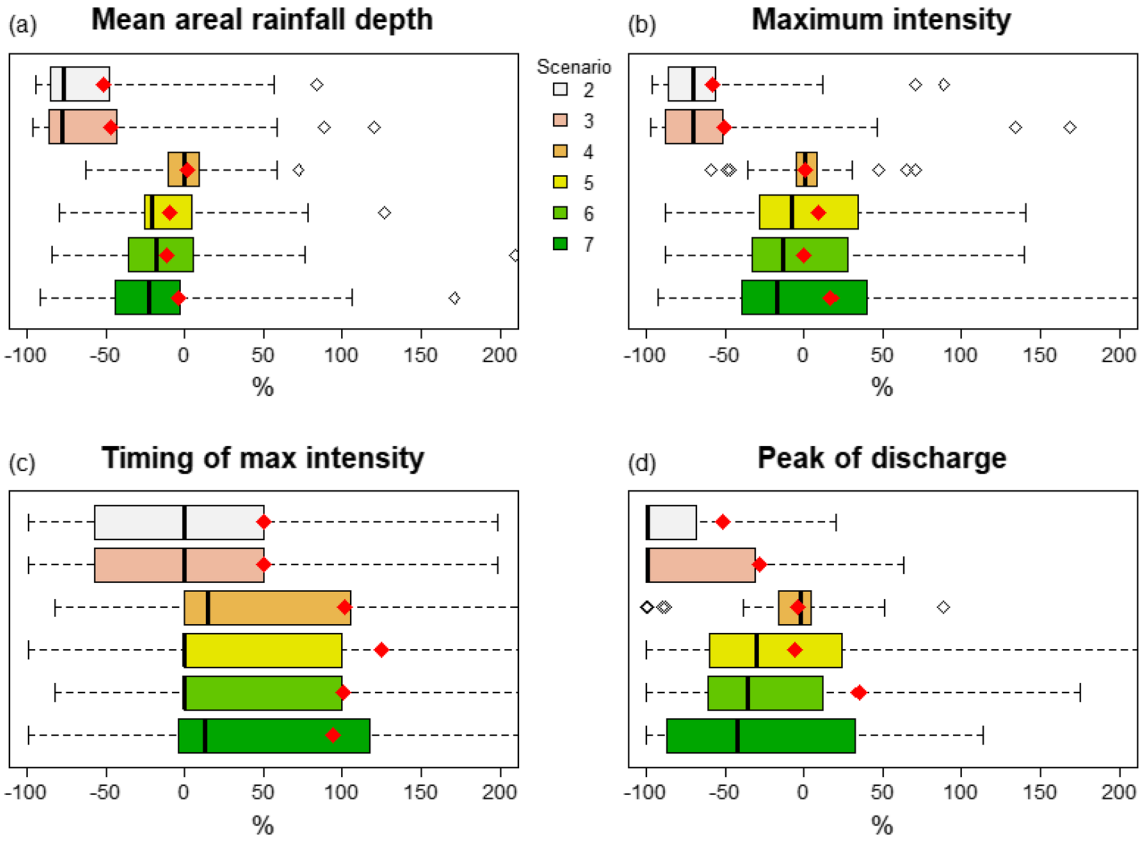


**Figure 3.** Boxplots of differences in (a) mean areal precipitation, (b) peak of discharge, (c) maximum intensity, and (d) timing of maximum intensity for each scenario compared with Scenario 1. Each boxplot refers to the values in Table 5. Circles are the outliers evaluated following Tukey (1977), the thick line in the boxplot difference is the average value excluded the outliers, the red diamond represents the average values considering all the events. For plotting purposes, some whiskers are not completely shown.

unadjusted radar data as rainfall input, they perform worse than using radar data corrected by using rain gauge records (Borga, 2002). Furthermore, for flash floods, using adequately corrected radar data as forcing, simulations better reproduce the recorded observations even compared to simulations which input are rain gauge data (Looper & Vieux, 2012). Our outcomes result slightly different; KED Scenarios, although using radar maps as forcing, produce worse results than using rain gauges.

No relationships have been found between the underestimation of raw radar-based rainfall fields and the considered watershed features (e.g., basin area, mean slope, antecedent moisture condition). These lacks of correlation are due to radar indirect measure of precipitation. Each rainfall event is different from another and, considering that rainfall reflectivity is directly related to its features (Atlas et al., 1999; Berne & Krajewski, 2013; Sempere-Torres et al., 1994), the use of a wrong *Z-R* relationship could lead to noticeable bias (Krajewski & Smith, 2002). In this case, the use of a *Z-R* relationship verified for convective events (Scenario 3) leads to results similar to Scenario 2. The use of correction techniques (Chumchean et al., 2004; Marra et al., 2014) should allow a better estimation of the real rainfall field. Unfortunately, they are much more time consuming and could hardly be used when real-time forecasting is requested. Otherwise, also a radar located closer to the basins subjected to DFs, with fewer beam blockages, could provide a more reliable estimation of the real rainfall field (Tiranti et al., 2014). Differences between peak discharges related to the different Scenarios are larger than those of the corresponding rainfalls. This occurs because of the short duration of rainfalls and the higher percentage of the losses (initial abstraction and infiltrated precipitation) so that a small difference of 3–5 mm can entail a sensible difference on both peak and volume of runoff (runoff coefficients of data of Gregoretti et al., 2016 and Berti et al., 2020 are smaller than 0.1). Moreover, when

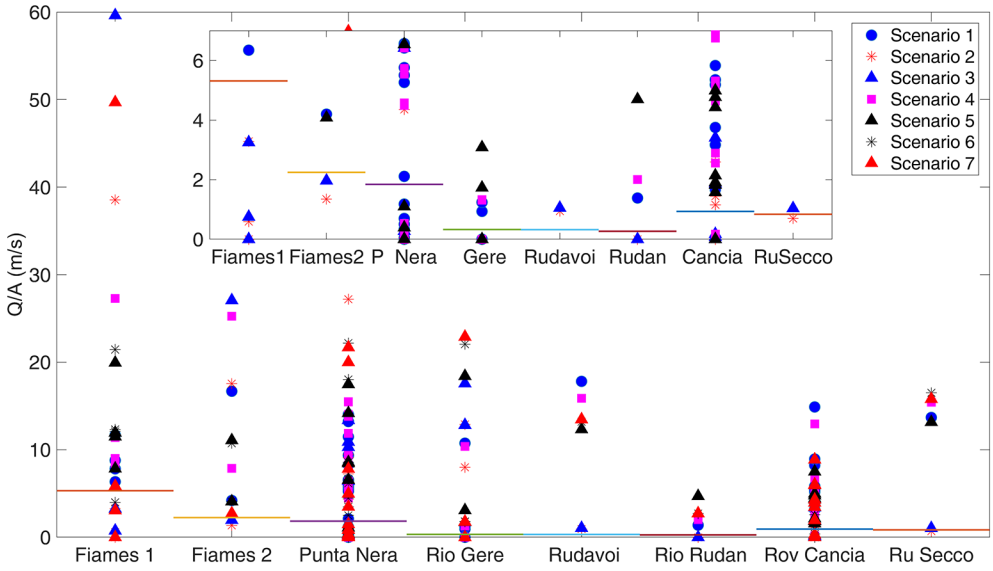


**Figure 4.** Comparison between the simulated peak runoff and the critical discharges values (horizontal segments) provided by Equation 10 for the watershed hits by debris flows. The insert zooms the simulated peak values that do not exceed the threshold. Rescaling of runoff with the basin area, *A*, was done for plotting purpose.

differences between precipitations result over 100%, differences between discharges could result greater than 1,000% due to the nonlinearity of the runoff-generation process (Robinson et al., 1995).

Regarding the triggering of DFs, Figure 4 shows for each basin the comparison between simulated and critical discharges computed according to Equation 10. Considering Scenarios 1 and 4, simulated peak runoff correctly predicts 33 and 32 DFs on 41 (80% and 78%, respectively), whereas those corresponding to Scenario 5 are 27 on 35 (77%). The prediction rates of Scenarios 6 and 7 are lower, 27 on 41 (66%). About 70% of the simulated peak discharge corresponding to Scenarios 2 and 3 are smaller than critical discharges computed by Equation 10 so that only 13 DF events are properly predicted. The events that Scenario 1 could not predict are DFs that occurred in the Punta Nera basin. Here, the nearest reference rain gauge is about 0.9 km far from the basin centroid. This distance could make recorded depths less representative of the rainfall fallen in the basin. On the other hand, in this basin, the radar beam clogging is less pronounced and could better estimate precipitations. For these reasons, for some events, rainfalls of Scenario 1 lead to simulated peak discharge smaller than the critical discharge, while corresponding rainfalls evaluated with other Scenarios result much larger than the critical discharge, pointing out the potential usefulness of radar data when the effects of the source errors are reduced. Although the simplified KED (Scenario 6) underestimates both rainfall and simulated discharges, its results are not so different from the more rigorous KED method. Scenario 7 deserves a separate discussion: its percentage of prediction is quite low and highlights the need to have a widespread network of rain gauges in a so complex area. Scenario 4 results in the best predictor but, on the other side, requires to maintain the network of rain gauges in the proximity of DF triggering areas (as we will highlight in Subsection 4.4).

Regarding the prediction of DF occurrence timings, we analyzed two cases: (a) DF occurrence time corresponding to the timing when simulated discharge overpasses the triggering threshold (Figure 5a); (b) DF occurrence time corresponding to the peak of the simulated discharge (Figure 5b). In both cases, scenarios show a good correspondence between observation and simulation timings (reported in the Supporting Information Material). Most of the events are predicted in a ±5-min time lag. In case (a) Scenario 1 tends to forecast DFs too early (in four events, the time lag is greater than 10 min in advance). The worst performances are obtained by raw-radar (the events are predicted with a time lag equal to or greater than 10 min). The other Scenarios have good timing (on average time lags lie in the range ±2 min). In case (b), Scenario 1 improves its prediction times, while the others tend to predict with delay (on average 2 min) the triggering of DFs (only two events are predicted in advance). However, the prediction in advance is not surprising

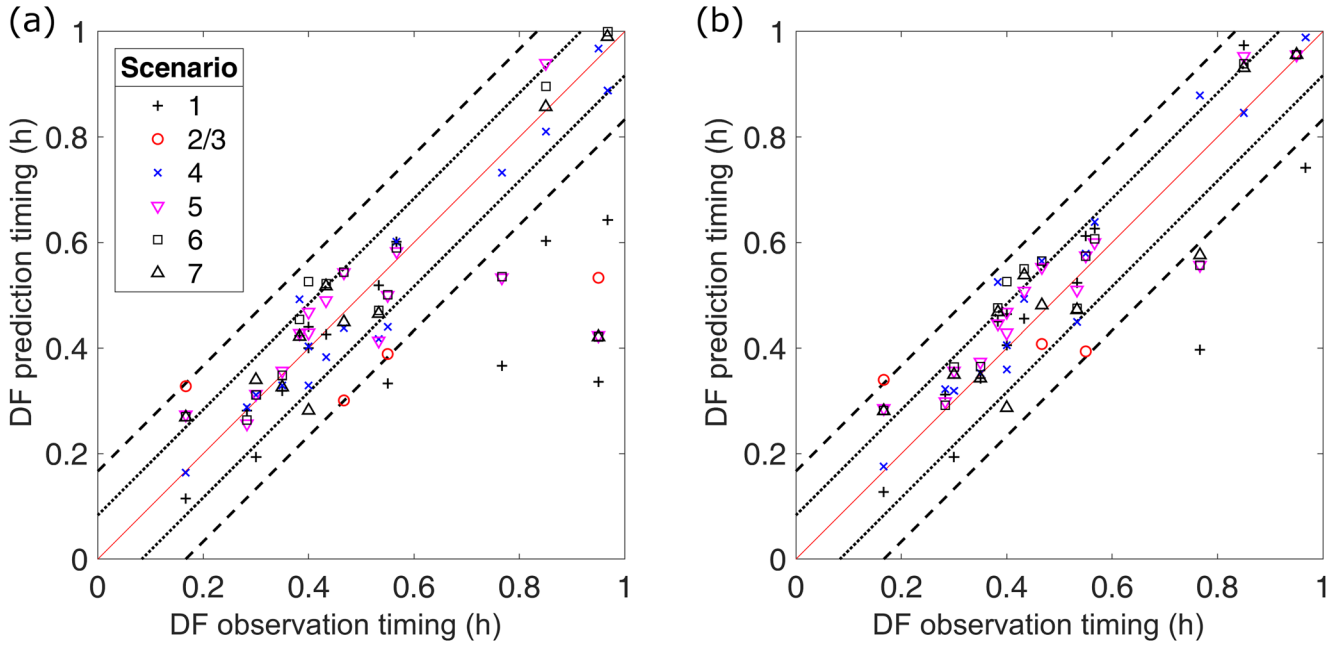


**Figure 5.** Comparison between the observed time of DFs occurrence and the simulated one. In the panels, the simulated time corresponds to the timing when the simulated discharge: (a) overpasses the triggering threshold, (b) reaches the peak of the discharge. Dotted and dashed lines indicate a 5-min and a 10-min lag with respect to the 1:1 line (red line), respectively. DF, debris flow.

because the DF formation, that is, the entrainment process of large quantities of sediments into runoff, could require some minutes.

As the last analysis, for the basins with more than 2 recorded DFs, we evaluated the correction factor (CF) from one rainstorm to another (defined as the ratio between cumulative depths of Scenarios 1 and 2). CFs consistently vary for every analyzed basin, further demonstrating how variable radar precipitation estimates are also in the same location (Figures 6a and 6b). However, a reasonable correlation between mean areal precipitation and CF has been found for each basin (Figure 6a): the lower the cumulative precipitation estimated by radar, the greater the CF. This result should be encouraging, especially for the high value of the various coefficients of determination, greater than 0.85 for every basin. It could provide an empirical-based operative method that could be generalized and used at other sites or for groups of neighboring basins, that is, (1) installing a rain gauge in the proximity of the basin, (2) fitting a relation between cumulative depths and CFs, (3) applying the fitting equation to future events. The same procedure has been carried out by fitting a power function on the full data set (Figure 6b). This interpolation has a greater degree of approximation, given that the value of the coefficient of determination is around 0.55. By multiplying the Scenario 2 maps by the relative site-specific or the global CFs, the results on modeling of DF triggering are better than those obtained with Scenarios 1 and 2: on 37 events, specific and global CF adjustments lead to 34 and 33 forecast DFs in comparison to 29 and 11 of Scenarios 1 and 2, respectively. The global CF function has been verified on the basins not used in its development, that is, those with only one or two DF events (Fiames 2, Rio Rudan, and Ru Secco). All the four DF events have been correctly predicted (two more than Scenario 2), proving good robustness of the tested procedure (detailed outcomes are reported in Supporting Information Material).

Unfortunately, this approach is lacking since the cumulative depth that the radar will estimate during an event is not known a priori. To overcome this issue, this application could be done auto-adjusting the CFs. Every 5 min, CFs should be updated based on the partial cumulative rainfall and hydrological simulations performed, paying attention to the values computed on the first time steps. In those instants, the radar cumulative precipitation tends to be very low and, consequently, the CF to be applied is very high (upper panels of Figure 6). A cumulative threshold could be adopted, that is, a minimum value for considering radar-recorded precipitation as significant; in this way, rainfalls of little interest will not be considered.

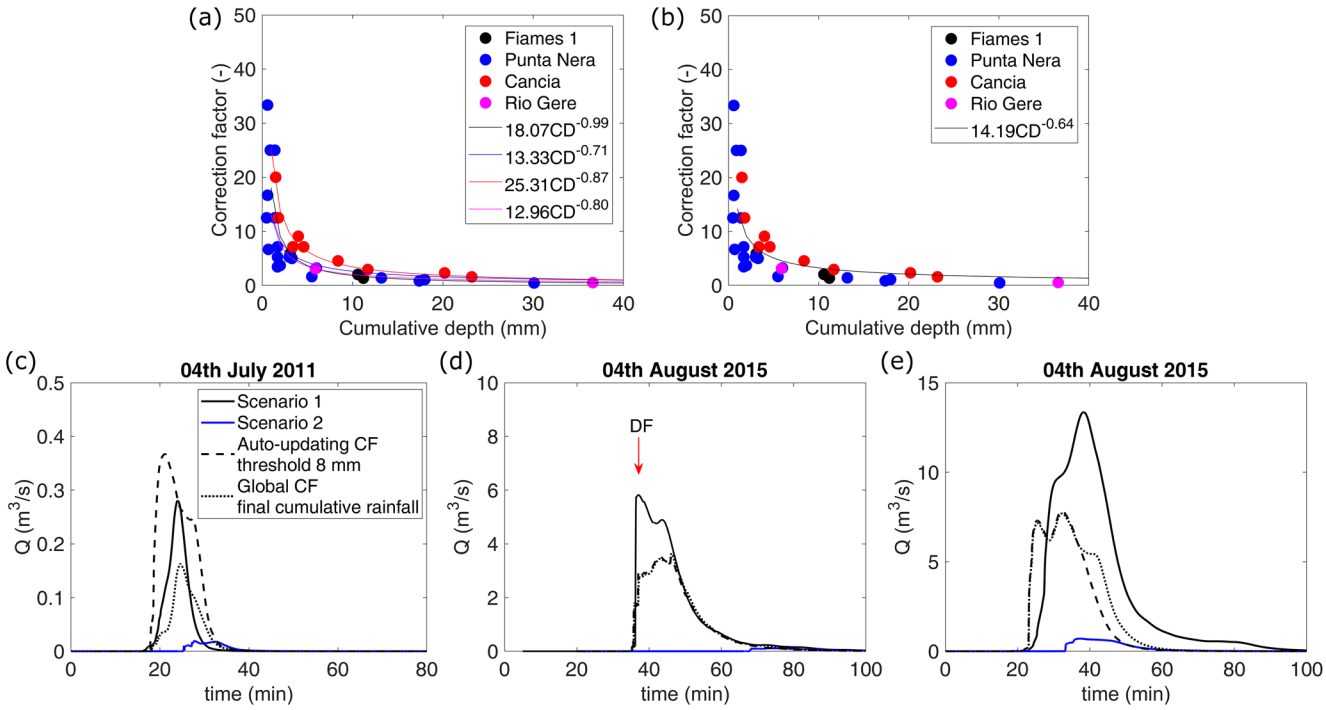


**Figure 6.** In upper panels, correction factors (CF) versus cumulative depths (CD) for the events of watersheds with more than 2 recorded DFs. In panel (a), we fit a different power function on data of each basin. In panel (b), we fit a power function on the entire data set of events. In lower panels, hydrological simulations of the event occurred on (c) July 4, 2011, in the Fiames 2 basin, and on August 4, 2015, in (d) the Rovina di Cancia and (e) the Rudan basins, respectively. Input rainfall data are Scenario 1, Scenario 2, Scenario 2 adjusted using the global CF evaluated when rainfall overcomes the critical cumulative threshold of 8 mm, and Scenario 2 adjusted using the global CF evaluated at the end of the precipitation. The timing of DF triggering is reported as an arrow for the event whose trigger has been monitored. DF, debris flow.

Taking for example the value of 8 mm as a critical threshold, almost half of the analyzed DF events, usually characterized by small magnitude (i.e., a small volume of transported sediments) are not considered. For the other events with much larger transported sediment volumes, once the set threshold was overcome, the auto-updating procedure can be carried out. Lower panels of Figure 6 show as examples the events that occurred on July 4, 2011 (Figure 6c) on the Fiames 2 basin, and on August 4, 2015, in the Rovina di Cancia (Figure 6d) and the Rudan (Figure 6e) basins, respectively. In general, after the auto-updating procedure, the discharge of hydrological simulations corresponding to events with radar cumulative rainfall larger than 8 mm overpasses the triggering threshold, whereas simulations performed using Scenario 2 maps do not always succeed in exceeding it. On the downside, the obtained peak values are quite different with respect to those obtained by Scenario 1. However, we must remember that considered precipitations are shorter than those used in the other simulations. Furthermore, these simulations do not differ too much from the simulations performed correcting the radar maps with the CF evaluated at the end of the precipitation (lasting longer). These results show that the hydrological model here applied can be used for determining the DF occurrence in early warning systems. Its operational use is guaranteed by the small time lag between the observed and predicted DF occurrence timings and its computational time shorter than 1 min. The high velocity of DF downstream routing requires an alert time as large as possible for implementing the safety procedures of civil protection.

### 4.4. Rescaling the Radar Field

In this section, we analyze how the choice of different rain gauges as ground truth could influence the results of simulations performed with radar data corrected through the Scenario 4 procedure (i.e., the corrected radar approach). The basins taken into account for this analysis are Fiames 1 and 2, and Rovina di Cancia (hereafter called Cancia). Fiames basins are two watersheds on the western slope of the Pomagagnon massif in the monitoring site A (Figure 7a). Cancia is located in the monitoring site B (Figure 7b), delimited by the

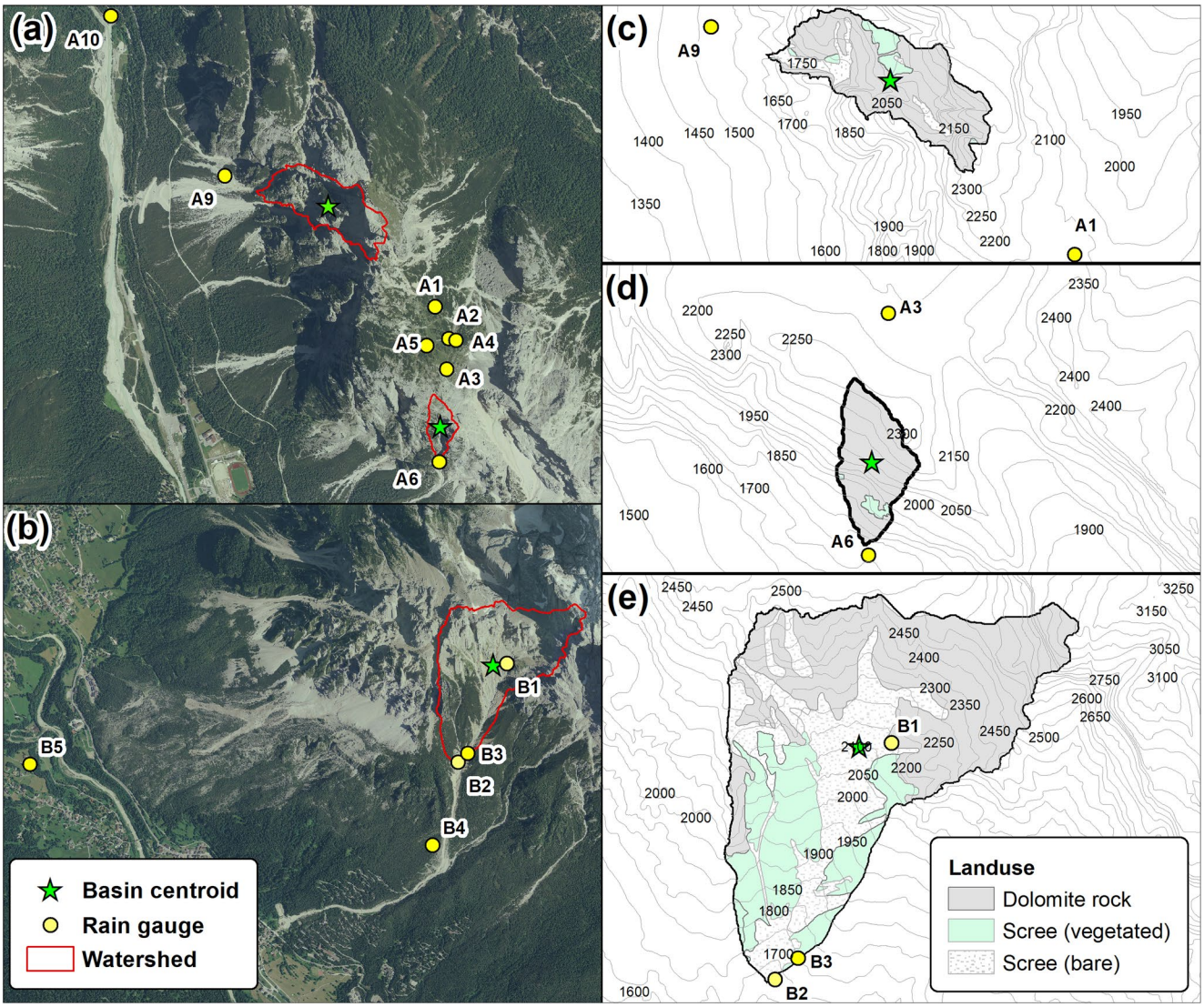


**Figure 7.** Orthophoto of the Fiames area (a) and the Cancia watershed (b); (c–e) The land cover of the basins Fiames 2, Fiames 1, and Cancia, respectively. Isolines represent isohypses.

western slope of Mt. Antelao. Furthermore, the Cancia basin is historically prone to stony DFs, that in the past inundated the village of Borca di Cadore causing several fatalities, as pointed out by several authors (Bacchini & Zannoni, 2003; Deganutti & Tecca, 2013; Simoni et al., 2020). This is the reason of the presence at Cancia of two permanent (B4 and B5) rain gauges managed by ARPAV, two rain gauges (B2 and B3) installed by the Universities of Bologna and Padova (Gregoretti et al., 2016; Simoni et al., 2020), and two rain gauges (B1a and B1b) of the monitoring and alarm system of the LPSB, since 2014. The abundance of gauges in both the areas with different distances from the watershed centroids permits to analyze how the choice of the reference gauge for the correction of radar rainfall (Scenario 4) influences both the corrected radar rainfall field and the simulated runoff discharges. For the Fiames basins, we choose the events that occurred in 2011 (both the basins) and 2015 (only Fiames 1), for Cancia we consider the DF events that occurred in 2015, 2018, and 2020 when data of rain gauge B1 (averaged values of B1a and B1b) are available. The rain gauges available at Fiames are A1, A6, and A10 for the events of 2011 and A3, A6, and A10 for the events of 2015. The rain gauges available at Cancia are B1, B2, B4, and B5 for all the events.

In Figure 8, for each event, we plot the cumulative rainfall recorded by each considered rain gauge and estimated by radar in the corresponding locations. It is interesting pointing out that the spread between the depths

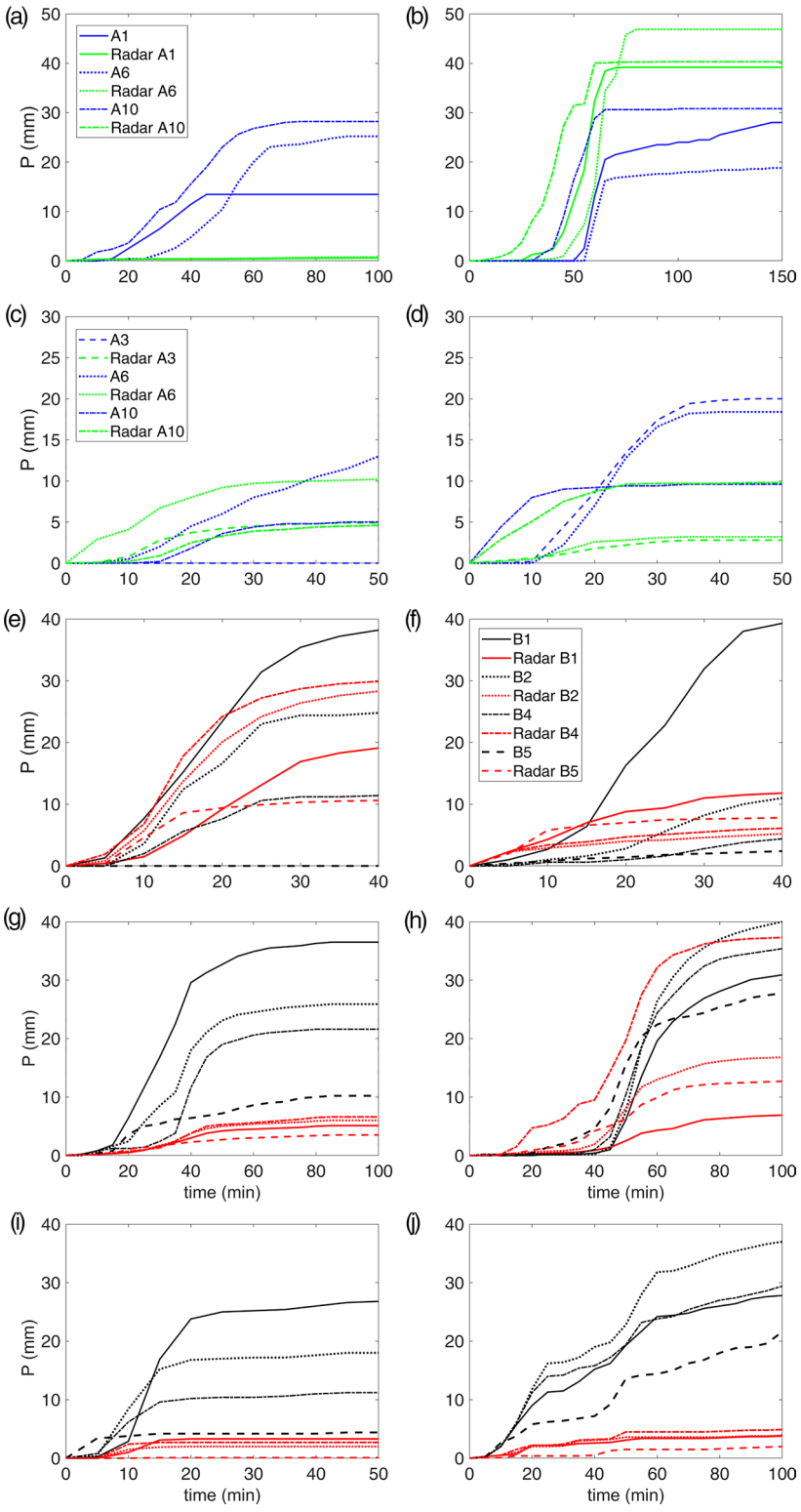


**Figure 8.** Precipitations recorded by rain gauges during the DF events occurred on 2011, (a) July 4, (b) August 18; 2015, (c) June 7, (d) July 25, (e) July 23, (f) August 4, 2018, (g) July 5, (h) August 1, 2020, (i) July, 1, (j) August, 29. In the figure, we also report the cumulative depths estimated by radar in the corresponding locations (the same line style identifies corresponding rain gauge and radar depths). DF, debris flow.

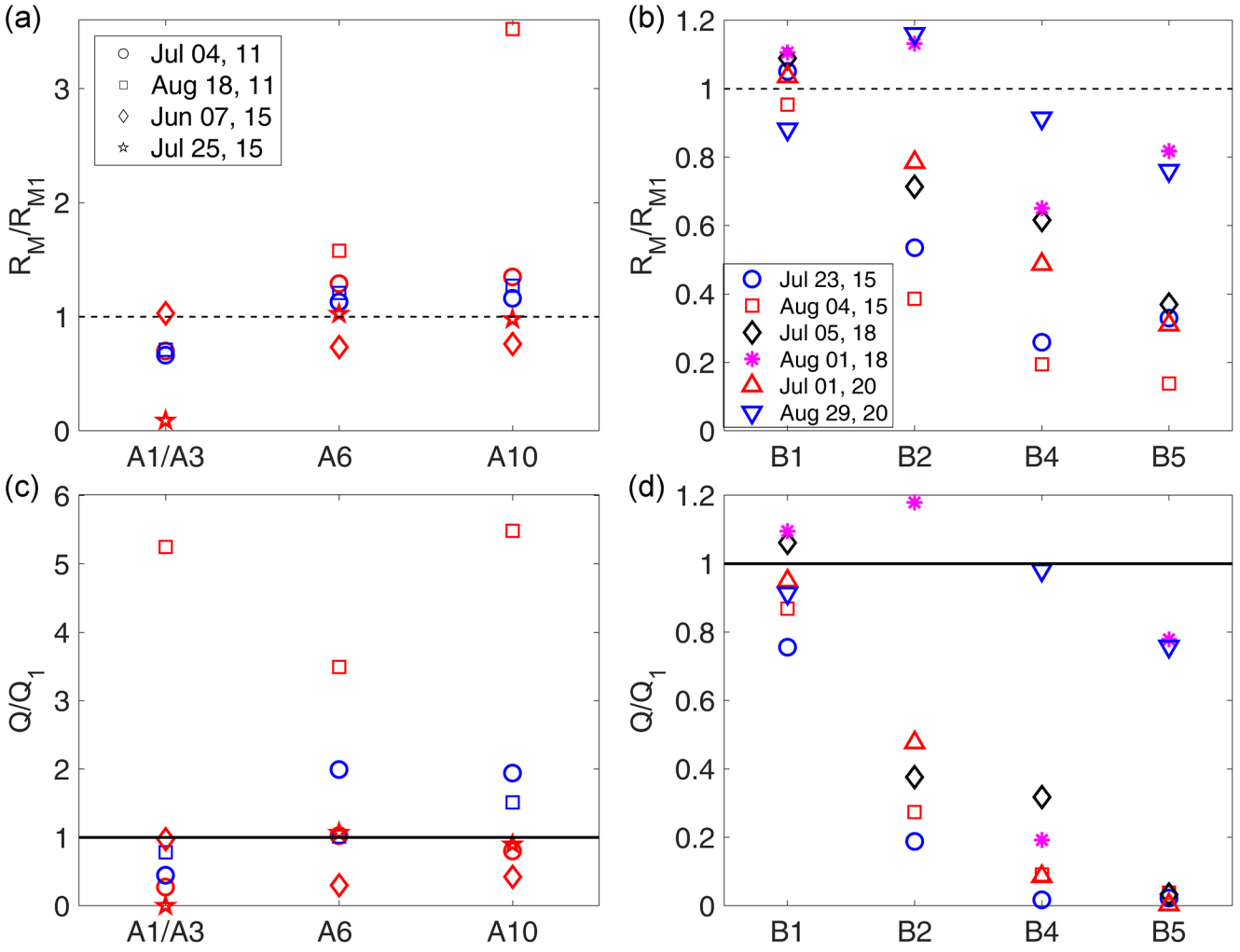


**Figure 9.** Comparison of the mean areal rainfall depth ($R_M$) and peak simulated discharges ($Q$) corresponding to Scenario 4 after using all the rain gauge as reference rain gauge in Fiames 1 (red markers) and 2 (blue markers) for the events of July 4 and August 18, 2011, and June 7 and July 25, 2015 (a and c), 2011, and in Rovina di Cancia (b and d) for the events of July 23 and August 4, 2015; July 5 and August 1, 2018; July 1 and August 29, 2020. The terms are rescaled with the correspondent Scenario 1 values, respectively, $R_{M1}$ and $Q_1$.

recorded by rain gauges is small for each event in the Fiames area, whereas in the Cancia area tends to be larger, despite the maximum distances and elevation gaps between gauges are comparable in the two monitoring sites. On the other hand, for both the sites the significance of radar estimates depends on the considered event.

Due to these marked differences in both rainfall depths and simulated discharges between Scenarios 1 and 2, we applied the Scenario 4 correction, using one by one the various rain gauges as reference gauge. Figure 9 compares the mean areal rainfall depth $R_M$ on the basins and the corresponding simulated peak discharges $Q$ after using different rain gauges for the Scenario 4 correction, normalized through data and results provided by Scenario 1 ($R_{M1}$ and $Q_1$).

The performed analysis shows as better estimations are obtained when the rain gauge nearest to the watershed centroid is used, independently from its location. For the events recorded in Fiames, better results are obtained when radar images are corrected by using the rain gauges A6 or A10; nevertheless, all the simulations but two (corrected by A1 rain gauge) can predict the triggering of DFs. The event of August 18, 2011, shows higher gaps between Scenario 1 and Scenario 4 due to the pre-existing difference between raw radar images and rain gauge measurements. For all the events, the worst performance of correcting images with the A1 rain gauge is probably due to its position beyond the ridge that delimits the hydrological

watersheds, even if, in the case of the Fiames 2 basin, it is closer than A10 to the centroid of the catchment. Storms traveling from West to East mostly unload on the basin and, getting over the ridge, their intensity decreases. Consequently, the correction with a rain gauge far from the core of the precipitation could lead to a high error. The case of Cancia is a bit different. Differences between mean areal rainfall depths of Scenarios 4 and 1 for the events vary in the range −11%–10%, and between −61% and 16% when using the rain gauges B1 and B2 respectively. In the case of the B4 and B5, these values range from −81% to −8% and from −86% to −18%, respectively. The corresponding differences for the simulated peak discharges vary between −24% and 10% in the case of B1, and in the range −81%–84%, in the case of B2. A larger underestimation in simulated peak runoff occurs when using B4 and B5. In these cases, the differences generally stand over 80%, and the critical discharge threshold is overpassed only for the events that occurred on August 1, 2018, and on August 29, 2020. These exceptions occurred because, in these events, the greatest cumulative rainfalls were recorded by the B2 rain gauge and the precipitation depths recorded by B3 were comparable or greater than the B1 ones. Therefore, the use of corrected radar rainfall by using rain gauges far from the centroid could lead to a possible high underestimation of rainfall depths and simulated peak discharges, which could result in not able to provide the hydrological conditions required for the DF initiation processes.

## 5. Conclusions

The differences between rain gauge and radar-rainfall estimates and the use of different methods for correcting the radar images are studied to simulate the hydrologic DF triggering conditions. Results show that for the hydrological modeling of critical discharges of DF initiation, the use of rain gauges close or inside the DF-prone basin appears the better solution. Raw-radar data well capture the spatial variability of rainfalls but usually underestimate depths and intensities. The use of radar-rainfall fields does not allow the reproduction of the runoff required for the DF triggering, except in the Punta Nera basin, where radar beam is only marginally shielded by reliefs, at most up to 500 m. Radar-rainfall maps are therefore corrected following two methods: the former is the rescaling of radar-rainfall estimates employing the measured rainfall of a reference gauge (corrected radar approach), the latter is the KED (using different degrees of approximation). The corrected radar approach allows a better approximation of the rainfall field obtained by using the nearest neighbor interpolation of rain gauges, resulting in similar triggering discharges. KED shows worse performances, both in basin mean areal rainfalls and in simulated peak discharges. Nevertheless, both the methods have a similar rate on predicting the triggering of occurred DF events, twice the percentage resulting from the use of raw radar-rainfall data. The weaknesses of these methods are the restricted validity of the corrected radar approach (higher the distance between the reference gauge and the centroid of the basin closed at the DF initiation area, higher the probability to fail the simulation of the hydrological triggering conditions), whereas the main limitation for the employment of KED approach is the need of a linear relation between ground-recorded and radar rainfalls to obtain the rain fields. The corrected radar approach gives more certainties when the reference gauge used for the correction is located as much as possible close to the centroid and not beyond a ridge, while the KED one is better for a more general view in the whole area due to the use of more rain gauges. The use of simplified versions of KED could give decent results despite their degree of approximation. A potential solution could be the development of a basin-specific or a global relation, centered on a CF to be applied to the radar maps of each event. In this way, the rate of prediction of DFs results better than other methods, also in the basins not used for developing the global corrective function. Unfortunately, this approach is still lacking since the radar cumulative depth of each event, necessary to estimate the CF, is difficult to establish a priori. To overcome this problem, CFs can be auto-updated during the events and hydrological simulations consequently performed. Such an empiric approach can be applied when the cumulative-depth estimated by the radar exceeds a threshold usually corresponding to DF events of medium-high magnitude, and in these cases, it allows the prediction of all the occurred DFs. However, this methodology should be deeper tested, both in this and in other geological and environmental contexts. In conclusion, outcomes highlight that, at the moment, in this area, it is essential to maintain at least a rain gauge, as close as possible to the centroid of the basin contributing to the DF initiation area because radar estimates are not always suitable for hydrological modeling. However, using these networks, it is possible to develop a radar-data correction approach that allows the correction of data also in case of malfunction of the rain gauges. Anyway, the placement of a radar closer to the areas could improve the real-time estimation of rainfall field, to be used for the prediction of DF occurrence in early warning systems.

## Data Availability Statement

Data are archived in HydroShare, http://www.hydroshare.org/resource/de564970a2924bcc8eb04cfd75e19f60.

**Acknowledgments**
This work was supported by the following projects: "INADEF (Innovative eArly warning system for Debris Flow)" funded by the Interregional program Italy Austria of European Union; "GAP-DEMM (GIS-based integrated platform for Debris Flow Monitoring, Modeling and Hazard Mitigation", funded by CARIPARO foundation); "PARAmount (imProved Accessibility: Reliability and security of Alpine transport infrastructure related to mountainous hazards in a changing climate)" funded by Alpine Space program of European Union; "Study of new early warning systems against hydrogeological risk and their social perception in a high valuable area for tourism and environment" funded by the University of Padova (Grant no. CPDA119318); "Forecasting of hazardous mass movement phenomena in the current climate change" funded by the Italian Ministry of Education, University and Research; "Hydrological modeling of runoff due to convective rainfalls in the initiation area of debris flows" funded by the University of Padova. The authors wish to thank the Regional Agency for Environmental Prevention and Protection of Veneto and the Hydrographic Office of Autonomous Province of Bolzano for the meteorological data; the Department Land Defense and Civil Protection of the Province of Belluno both for the meteorological and LiDAR 2011 data; the association "Regole d'Ampezzo," that permitted to set up rain gauges and monitoring stations and provided the 2010 Lidar data; the Public Work Department of Veneto Region for the LiDAR 2015 data; M. Berti and A. Simoni for their fundamental help in setting up the monitoring stations; B. Bayer, L. Bertello, P. Ciuffi, G. Crucil, G. De Vido, I. Fent, M. Morandi, A. Pimazzoni, and G. Squarzoni for their help in the field; F. Marra for his useful suggestions; and M. Tollardo and M. Munari for their patience and courtesy.

## References

Ahmed, S., & De Marsily, G. (1987). Comparison of geostatistical methods for estimating transmissivity using data on transmissivity and specific capacity. *Water Resources Research*, *23*(9), 1717–1737. https://doi.org/10.1029/WR023i009p01717

Anagnostou, M. N., Kalogiros, J., Anagnostou, E. N., Tarolli, M., Papadopoulos, A., & Borga, M. (2010). Performance evaluation of high-resolution rainfall estimation by X-band dual-polarization radar for flash flood applications in mountainous basins. *Journal of Hydrology*, *394*(1–2), 4–16. https://doi.org/10.1016/j.jhydrol.2010.06.026

Andrieu, H., Creutin, J.-D., Delrieu, G., & Faure, D. (1997). Use of a weather radar for the hydrology of a mountainous area. Part I: Radar measurement interpretation. *Journal of Hydrology*, *193*(1–4), 1–25. https://doi.org/10.1016/S0022-1694(96)03202-7

Atlas, D., Ulbrich, C. W., Marks, F. D., Amitai, E., & Williams, C. R. (1999). Systematic variation of drop size and radar-rainfall relations. *Journal of Geophysical Research*, *104*(D6), 6155–6169. https://doi.org/10.1029/1998JD200098

Bacchini, M., & Zannoni, A. (2003). Relations between rainfall and triggering of debris-flow: Case study of Cancia (Dolomites, Northeastern Italy). *Natural Hazards and Earth System Sciences*, *3*(1/2), 71–79. https://doi.org/10.5194/nhess-3-71-2003

Bathurst, J. C., Burton, A., Clarke, B. G., & Gallart, F. (2006). Application of the SHETRAN basin-scale, landslide sediment yield model to the Llobregat basin, Spanish Pyrenees. *Hydrological Processes*, *20*(14), 3119–3138. https://doi.org/10.1002/hyp.6151

Bathurst, J. C., Graf, W. H., & Cao, H. H. (1987). Bedload discharge equations for steep mountain rivers. In C. Thorne, J. Bathurst, & R. Hey (Eds.), *Sediment transport in gravel-bed rivers* (pp. 453–477). Chichester, UK: John Wiley & Sons.

Baum, R. L., & Godt, J. W. (2010). Early warning of rainfall-induced shallow landslides and debris flows in the USA. *Landslides*, *7*(3), 259–272. https://doi.org/10.1007/s10346-009-0177-0

Berger, C., McArdell, B. W., Fritschi, B., & Schlunegger, F. (2010). A novel method for measuring the timing of bed erosion during debris flows and floods. *Water Resources Research*, *46*, W02502. https://doi.org/10.1029/2009WR007993

Bernard, M., Berti, M., Simoni, A., & Gregoretti, C. (2019). Characteristics of debris flows just downstream the initiation area on Punta Nera cliffs, Venetian Dolomites. In J. W. Kean, J. A. Coe, P. M. Santi, & B. K. Guillen (Eds.), *Debris-flow hazards mitigation: Mechanics, monitoring, modeling, and assessment*. Golden, CO: Association of Environmental and Engineering Geologists.

Bernard, M., Boreggio, M., Degetto, M., & Gregoretti, C. (2019). Model-based approach for design and performance evaluation of works controlling stony debris flows with an application to a case study at Rovina di Cancia (Venetian Dolomites, Northeast Italy). *Science of the Total Environment*, *688*, 1373–1388. https://doi.org/10.1016/j.scitotenv.2019.05.468

Bernard, M., Underwood, S. J., Berti, M., Simoni, A., & Gregoretti, C. (2020). Observations of the atmospheric electric field preceding intense rainfall events in the Dolomite Alps near Cortina d'Ampezzo, Italy. *Meteorology and Atmospheric Physics*, *132*, 99–111. https://doi.org/10.1007/s00703-019-00677-6

Berne, A., & Krajewski, W. F. (2013). Radar for hydrology: Unfulfilled promise or unrecognized potential? *Advances in Water Resources*, *51*, 357–366. https://doi.org/10.1016/j.advwatres.2012.05.005

Berti, M., Bernard, M., Simoni, A., & Gregoretti, C. (2020). Physical interpretation of rainfall thresholds for runoff-generated debris flows. *Journal of Geophysical Research: Earth Surface*, *125*(6), e2019JF005513. https://doi.org/10.1029/2019JF005513

Berti, M., & Simoni, A. (2005). Experimental evidences and numerical modeling of debris flow initiated by channel runoff. *Landslides*, *2*(3), 171–182. https://doi.org/10.1007/s10346-005-0062-4

Borga, M. (2002). Accuracy of radar rainfall estimates for streamflow simulation. *Journal of Hydrology*, *267*(1–2), 26–39. https://doi.org/10.1016/S0022-1694(02)00137-3

Borga, M., Anagnostou, E. N., Blöschl, G., & Creutin, J.-D. (2010). Flash floods: Observations and analysis of hydro-meteorological controls. *Journal of Hydrology*, *394*(1–2), 1–284. https://doi.org/10.1016/j.jhydrol.2010.07.048

Borga, M., Degli Esposti, S., & Norbiato, D. (2006). Influence of errors in radar rainfall estimates on hydrological modeling prediction uncertainty. *Water Resources Research*, *42*, W02502. https://doi.org/10.1029/2005WR004559

Burrough, P. A., & McDonnell, R. A. (1998). *Principles of geographical information systems* (2nd ed.). New York: Oxford University Press.

Caine, N. (1980). The rainfall intensity: Duration control of shallow landslides and debris flows. *Geografiska Annaler. Series A, Physical Geography*, *62*(1/2), 23–27. https://doi.org/10.2307/520449

Cannon, S. H., Gartner, J. E., Wilson, R. C., Bowers, J. C., & Laber, J. L. (2008). Storm rainfall conditions for floods and debris flows from recently burned areas in southwestern Colorado and southern California. *Geomorphology*, *96*(3–4), 250–269. https://doi.org/10.1016/j.geomorph.2007.03.019

Chen, J., Brissette, F. P., Chaumont, D., & Braun, M. (2013). Finding appropriate bias correction methods in downscaling precipitation for hydrologic impact studies over North America. *Water Resources Research*, *49*(7), 4187–4205. https://doi.org/10.1002/wrcr.20331

Chumchean, S., Seed, A., & Sharma, A. (2004). Application of scaling in radar reflectivity for correcting range-dependent bias in climatological radar rainfall estimates. *Journal of Atmospheric and Oceanic Technology*, *21*(10), 1545–1556. http://doi.org/10.1175/1520-0426(2004)021⟨1545:AOSIRR⟩2.0.CO;2

Coe, J. A., Kinner, D. A., & Godt, J. W. (2008). Initiation conditions for debris flows generated by runoff at Chalk Cliffs, Central Colorado. *Geomorphology*, *96*(3–4), 270–297. https://doi.org/10.1016/j.geomorph.2007.03.017

Collins, F. C., & Bolstad, P. V. (1996). A comparison of spatial interpolation techniques in temperature estimation. *3rd International Conf/Workshop on Integrating GIS and Environmental Modeling* (pp. 122–134). Santa Fe, NM.

Cremonini, R., & Tiranti, D. (2018). The weather radar observations applied to shallow landslides prediction: A case study from north-western Italy. *Frontiers in Earth Science*, *6*, 1–12. https://doi.org/10.3389/feart.2018.00134

Creutin, J.-D., Delrieu, G., & Lebel, T. (1988). Rain measurement by raingage-radar combination: A geostatistical approach. *Journal of Atmospheric and Oceanic Technology*, *5*, 102–115. https://doi.org/10.1175/1520-0426(1988)005⟨0102:RMBRRC⟩2.0

Crosta, G. B., & Frattini, P. (2003). Distributed modeling of shallow landslides triggered by intense rainfall. *Natural Hazards and Earth System Sciences*, *3*(1/2), 81–93. https://doi.org/10.5194/nhess-3-81-2003

Cunha, L. K., Mandapaka, P. V., Krajewski, W. F., Mantilla, R., & Bradley, A. A. (2012). Impact of radar-rainfall error structure on estimated flood magnitude across scales: An investigation based on a parsimonious distributed hydrological model. *Water Resources Research*, *48*, W10515. https://doi.org/10.1029/2012WR012138

Cunha, L. K., Smith, J. A., Baeck, M. L., & Krajewski, W. F. (2013). An early performance evaluation of the NEXRAD dual-polarization radar rainfall estimates for urban flood applications. *Weather and Forecasting*, *28*(6), 1478–1497. https://doi.org/10.1175/WAF-D-13-00046.1

DeGaetano, A. T., & Wilks, D. S. (2009). Radar-guided interpolation of climatological precipitation data. *International Journal of Climatology*, *29*(2), 185–196. https://doi.org/10.1002/joc.1714

Deganutti, A. M., & Tecca, P. R. (2013). The case study of Cancia (Dolomites, Italy), a Mountain Village Threatened by a Debris Flow. In C. Margottini, P. Canuti, & K. Sassa (Eds), *Landslide science and practice* (pp. 329–333). Berlin, Heidelberg: Springer Berlin Heidelberg. https://doi.org/10.1007/978-3-642-31319-6_44

Degetto, M., Gregoretti, C., & Bernard, M. (2015). Comparative analysis of the differences between using LiDAR and contour-based DEMs for hydrological modeling of runoff generating debris flows in the Dolomites. *Frontiers in Earth Science*, *3*, 1–15. https://doi.org/10.3389/feart.2015.00021

Delrieu, G., Wijbrans, A., Boudevillain, B., Faure, D., Bonnifait, L., & Kirstetter, P. E. (2014). Geostatistical radar-rain gauge merging: A novel method for the quantification of rain estimation accuracy. *Advances in Water Resources*, *71*, 110–124. https://doi.org/10.1016/j.advwatres.2014.06.005

Destro, E., Amponsah, W., Nikolopoulos, E. I., Marchi, L., Marra, F., Zoccatelli, D., & Borga, M. (2018). Coupled prediction of flash flood response and debris flow occurrence: Application on an alpine extreme flood event. *Journal of Hydrology*, *558*, 225–237. https://doi.org/10.1016/j.jhydrol.2018.01.021

D'Agostino, V., Cesca, M., & Marchi, L. (2010). Field and laboratory investigations of runout distances of debris flows in the Dolomites (Eastern Italian Alps). *Geomorphology*, *115*(3–4), 294–304. https://doi.org/10.1016/j.geomorph.2009.06.032

D'Agostino, V., & Marchi, L. (2001). Debris flow magnitude in the Eastern Italian Alps: Data collection and analysis. *Physics and Chemistry of the Earth, Part C: Solar, Terrestrial and Planetary Science*, *26*(9), 657–663. https://doi.org/10.1016/S1464-1917(01)00064-2

Ehret, U. (2003). *Rainfall and flood nowcasting in small catchments using weather radar* (Doctoral thesis). Stuttgart: Universität.

Erdin, R. (2009). *Combining rain gauge and radar measurements of a heavy precipitation event over Switzerland: Comparison of geostatistical methods and investigation of important influencing factors* (Tech. Rep. No. 81). Zurich: MeteoSwiss.

Fehlmann, M., Rohrer, M., von Lerber, A., & Stoffel, M. (2020). Automated precipitation monitoring with the Thies disdrometer: Biases and ways for improvement. *Atmospheric Measurement Techniques*, *13*(9), 4683–4698. https://doi.org/10.5194/amt-13-4683-2020

Floris, M., D'Alpaos, A., Squarzoni, C., Genevois, R., & Marani, M. (2010). Recent changes in rainfall characteristics and their influence on thresholds for debris flow triggering in the Dolomitic area of Cortina d'Ampezzo, north-eastern Italian Alps. *Natural Hazards and Earth System Sciences*, *10*(3), 571–580. https://doi.org/10.5194/nhess-10-571-2010

Franceschinis, C., Thiene, M., Mattea, S., & Scarpa, R. (2020). Do information and citizens characteristics affect public acceptability of landslide protection measures? A latent class approach. In W. Leal Filho & D. Jacob (Eds), *Climate change management* (pp. 503–513). Springer. https://doi.org/10.1007/978-3-030-36875-3_25

Fulton, R. A., Breidenbach, J. P., Seo, D.-J., Miller, D. A., & O'Bannon, T. (1998). The WSR-88D rainfall algorithm. *Weather and Forecasting*, *13*(2), 377–395. https://doi.org/10.1175/1520-0434(1998)013⟨0377:TWRA⟩2.0.CO;2

Gatter, R., Cavalli, M., Crema, S., & Bossi, G. (2018). Modeling the dynamics of a large rock landslide in the Dolomites (eastern Italian Alps) using multi-temporal DEMs. *PeerJ*, *6*, e5903. https://doi.org/10.7717/peerj.5903

Germann, U., Galli, G., Boscacci, M., & Bolliger, M. (2006). Radar precipitation measurement in a mountainous region. *Quarterly Journal of the Royal Meteorological Society*, *132*(618), 1669–1692. https://doi.org/10.1256/qj.05.190

Gjertsen, U., Salek, M., & Michelson, D. (2004). Gauge adjustment of radar-based precipitation estimates in Europe. *Proceedings of ERAD*, 7–11.

Gong, L., Tang, C., Xiong, J., & Li, N. (2020). Debris flow generation based on critical discharge: A case study of Xiongmao Catchment, Southwestern China. *Water*, *12*(2), 552. https://doi.org/10.3390/w12020552

Goovaerts, P. (1997). *Geostatistics for natural resources evaluation*. Oxford University Press.

Goovaerts, P. (1999). Geostatistics in soil science: State-of-the-art and perspectives. *Geoderma*, *89*(1–2), 1–45. https://doi.org/10.1016/S0016-7061(98)00078-0

Goovaerts, P. (2000). Geostatistical approaches for incorporating elevation into the spatial interpolation of rainfall. *Journal of Hydrology*, *228*(1–2), 113–129. https://doi.org/10.1016/S0022-1694(00)00144-X

Gregoretti, C., & Dalla Fontana, G. (2007). Rainfall threshold for the initiation of debris flows by channel-bed failure in the Dolomites. In C. Chen, & J. J. Major (Eds.), *Debris-flow mitigation: Mechanics, prediction and assessment* (pp. 11–21). Milpress.

Gregoretti, C., & Dalla Fontana, G. (2008). The triggering of debris flow due to channel-bed failure in some alpine headwater basins of the Dolomites: Analyses of critical runoff. *Hydrological Processes*, *22*(13), 2248–2263. https://doi.org/10.1002/hyp.6821

Gregoretti, C., Degetto, M., Bernard, M., Crucil, G., Pimazzoni, A., De Vido, G., et al. (2016). Runoff of small rocky headwater catchments: Field observations and hydrological modeling. *Water Resources Research*, *52*(10), 8138–8158. https://doi.org/10.1002/2016WR018675

Guzzetti, F., Peruccacci, S., Rossi, M., & Stark, C. P. (2008). The rainfall intensity-duration control of shallow landslides and debris flows: An update. *Landslides*, *5*(1), 3–17. https://doi.org/10.1007/s10346-007-0112-1

Haberlandt, U. (2007). Geostatistical interpolation of hourly precipitation from rain gauges and radar for a large-scale extreme rainfall event. *Journal of Hydrology*, *332*(1–2), 144–157. https://doi.org/10.1016/j.jhydrol.2006.06.028

Habib, E., Aduvala, A. V., & Meselhe, E. A. (2008). Analysis of radar-rainfall error characteristics and implications for streamflow simulation uncertainty. *Hydrological Sciences Journal*, *53*(3), 568–587. https://doi.org/10.1623/hysj.53.3.568

Hartkamp, A. D., De Beurs, K., Stein, A., & White, J. W. (1999). *Interpolation techniques for climate variables*. Mexico, D.F. CIMMYT.

Hasan, M. M., Sharma, A., Johnson, F., Mariethoz, G., & Seed, A. (2014). Correcting bias in radar ZR relationships due to uncertainty in point rain gauge networks. *Journal of Hydrology*, *519*(PB), 1668–1676. https://doi.org/10.1016/j.jhydrol.2014.09.060

Hasan, M. M., Sharma, A., Johnson, F., Mariethoz, G., & Seed, A. (2016). Merging radar and in situ rainfall measurements: An assessment of different combination algorithms. *Water Resources Research*, *52*(10), 8384–8398. https://doi.org/10.1002/2015WR018441

Höhle, J., & Höhle, M. (2009). Accuracy assessment of digital elevation models by means of robust statistical methods. *ISPRS Journal of Photogrammetry and Remote Sensing*, *64*(4), 398–406. https://doi.org/10.1016/j.isprsjprs.2009.02.003

Holawe, F., & Dutter, R. (1999). Geostatistical study of precipitation series in Austria: Time and space. *Journal of Hydrology*, *219*(1–2), 70–82. https://doi.org/10.1016/S0022-1694(99)00046-3

Hürlimann, M., Abancó, C., Moya, J., & Vilajosana, I. (2014). Results and experiences gathered at the Rebaixader debris-flow monitoring site, Central Pyrenees, Spain. *Landslides*, *11*(6), 939–953. https://doi.org/10.1007/s10346-013-0452-y

Innes, J. L. (1983). Debris flows. *Progress in Physical Geography*, *7*(4), 469–501. https://doi.org/10.1177/030913338300700401

Jakob, M., & Hungr, O. (2005). *Debris-flow hazards and related phenomena*. Berlin, Heidelberg: Springer Berlin Heidelberg. https://doi.org/10.1007/b138657

Kean, J. W., McCoy, S. W., Tucker, G. E., Staley, D. M., & Coe, J. A. (2013). Runoff-generated debris flows: Observations and modeling of surge initiation, magnitude, and frequency. *Journal of Geophysical Research: Earth Surface*, *118*(4), 2190–2207. https://doi.org/10.1002/jgrf.20148

Krajewski, W. F. (1987). Cokriging radar-rainfall and rain gage data. *Journal of Geophysical Research*, *92*, 9571. https://doi.org/10.1029/JD092iD08p09571

Krajewski, W. F., & Smith, J. A. (2002). Radar hydrology: Rainfall estimation. *Advances in Water Resources*, *25*(8–12), 1387–1394. https://doi.org/10.1016/S0309-1708(02)00062-3

Krajewski, W. F., Villarini, G., & Smith, J. A. (2010). RADAR-rainfall uncertainties. *Bulletin of the American Meteorological Society*, *91*(1), 87–94. https://doi.org/10.1175/2009BAMS2747.1

Looper, J. P., & Vieux, B. E. (2012). An assessment of distributed flash flood forecasting accuracy using radar and rain gauge input for a physics-based distributed hydrologic model. *Journal of Hydrology*, *412–413*, 114–132. https://doi.org/10.1016/j.jhydrol.2011.05.046

Ly, S., Charles, C., & Degré, A. (2013). Different methods for spatial interpolation of rainfall data for operational hydrology and hydrological modeling at watershed scale: A review. *Base*, *17*(2), 392–406.

Marchi, L., Dalla Fontana, G., Cavalli, M., & Tagliavini, F. (2008). Rocky headwaters in the Dolomites, Italy: Field observations and topographic analysis. *Artic, Antarctic, and Alpine Research*, *40*(4), 685–694. https://doi.org/10.1657/1523-0430(07-037

Marra, F., Nikolopoulos, E. I., Creutin, J.-D., & Borga, M. (2014). Radar rainfall estimation for the identification of debris-flow occurrence thresholds. *Journal of Hydrology*, *519*, 1607–1619. https://doi.org/10.1016/j.jhydrol.2014.09.039

Marshall, J. S., & Palmer, W. M. K. (1948). The distribution of raindrops with size. *Journal of Meteorology*, *5*(4), 165–166. https://doi.org/10.1175/1520-0469(1948)005⟨0165:TDORWS⟩2.0.CO;2

Masson, D., & Frei, C. (2014). Spatial analysis of precipitation in a high-mountain region: Exploring methods with multi-scale topographic predictors and circulation types. *Hydrology and Earth System Sciences*, *18*(11), 4543–4563. https://doi.org/10.5194/hess-18-4543-2014

Mattea, S., Franceschinis, C., Scarpa, R., & Thiene, M. (2016). Valuing landslide risk reduction programs in the Italian Alps: The effect of visual information on preference stability. *Land Use Policy*, *59*, 176–184. https://doi.org/10.1016/j.landusepol.2016.08.032

McGuire, L. A., & Youberg, A. M. (2020). What drives spatial variability in rainfall intensity-duration thresholds for post-wildfire debris flows? Insights from the 2018 Buzzard Fire, NM, USA. *Landslides*, *17*, 2385–2399. https://doi.org/10.1007/s10346-020-01470-y

Neary, V. S., Habib, E., & Fleming, M. (2004). Hydrologic modeling with NEXRAD precipitation in Middle Tennessee. *Journal of Hydrologic Engineering*, *9*(5), 339–349. https://doi.org/10.1061/(ASCE)1084-0699

Nikolopoulos, E. I., Borga, M., Creutin, J.-D., & Marra, F. (2015). Estimation of debris flow triggering rainfall: Influence of rain gauge density and interpolation methods. *Geomorphology*, *243*, 40–50. https://doi.org/10.1016/j.geomorph.2015.04.028

Nikolopoulos, E. I., Crema, S., Marchi, L., Marra, F., Guzzetti, F., & Borga, M. (2014). Impact of uncertainty in rainfall estimation on the identification of rainfall thresholds for debris flow occurrence. *Geomorphology*, *221*, 286–297. https://doi.org/10.1016/j.geomorph.2014.06.015

Orlandini, S., & Morlini, I. (2000). Artificial neural network estimation of rainfall intensity from radar observations. *Journal of Geophysical Research*, *105*(D20), 24849–24861. https://doi.org/10.1029/2000JD900408

Orlandini, S., & Rosso, R. (1996). Diffusion wave modeling of distributed catchment dynamics. *Journal of Hydrologic Engineering*, *1*(3), 103–113. https://doi.org/10.1061/(ASCE)1084-0699

Palau, R. M., Hürlimann, M., Berenguer, M., & Sempere-Torres, D. (2020). Influence of the mapping unit for regional landslide early warning systems: comparison between pixels and polygons in Catalonia (NE Spain). *Landslides*, *17*(9), 2067–2083. https://doi.org/10.1007/s10346-020-01425-3

Papa, M. N., Medina, V., Ciervo, F., & Bateman, A. (2013). Derivation of critical rainfall thresholds for shallow landslides as a tool for debris flow early warning systems. *Hydrology and Earth System Sciences*, *17*(10), 4095–4107. https://doi.org/10.5194/hess-17-4095-2013

Pastorello, R., D'Agostino, V., & Hürlimann, M. (2020). Debris flow triggering characterization through a comparative analysis among different mountain catchments. *Catena*, *186*, 104348. https://doi.org/10.1016/j.catena.2019.104348

Piton, G., & Recking, A. (2016). Design of sediment traps with open check dams. I: Hydraulic and deposition processes. *Journal of Hydraulic Engineering*, *142*(2), 04015045. https://doi.org/10.1061/(ASCE)HY.1943-7900.0001048

Rabiei, E., & Haberlandt, U. (2015). Applying bias correction for merging rain gauge and radar data. *Journal of Hydrology*, *522*, 544–557. https://doi.org/10.1016/j.jhydrol.2015.01.020

Raymond, C. A., McGuire, L. A., Youberg, A. M., Staley, D. M., & Kean, J. W. (2020). Thresholds for postwildfire debris flows: Insights from the Pinal Fire, Arizona, USA. *Earth Surface Processes and Landforms*, *45*(6), 1349–1360. https://doi.org/10.1002/esp.4805

Reid, M. E., Coe, J. A., & Brien, D. L. (2016). Forecasting inundation from debris flows that grow volumetrically during travel, with application to the Oregon Coast Range, USA. *Geomorphology*, *273*, 396–411. https://doi.org/10.1016/j.geomorph.2016.07.039

Rendon, S. H., Vieux, B. E., & Pathak, C. S. (2013). Continuous forecasting and evaluation of derived Z-R relationships in a Sparse Rain Gauge Network Using NEXRAD. *Journal of Hydrologic Engineering*, *18*(2), 175–182. https://doi.org/10.1061/(ASCE)HE.1943-5584.0000579

Rengers, F. K., McGuire, L. A., Kean, J. W., Staley, D. M., & Hobley, D. E. J. (2016). Model simulations of flood and debris flow timing in steep catchments after wildfire. *Water Resources Research*, *52*(8), 6041–6061. https://doi.org/10.1002/2015WR018176

Restrepo, P., Jorgensen, D. P., Cannon, S. H., Costa, J., Laber, J., Major, J., et al. (2008). Joint NOAA/NWS/USGS prototype debris flow warning system for recently burned areas in Southern California. *Bulletin of the American Meteorological Society*, *89*(12), 1845–1852. https://doi.org/10.1175/2008BAMS2416.1

Robinson, J. S., Sivapalan, M., & Snell, J. D. (1995). On the relative roles of hillslope processes, channel routing, and network geomorphology in the hydrologic response of natural catchments. *Water Resources Research*, *31*(12), 3089–3101. https://doi.org/10.1029/95WR01948

Sapriza-Azuri, G., Jódar, J., Navarro, V., Slooten, L. J., Carrera, J., & Gupta, H. V. (2015). Impacts of rainfall spatial variability on hydrogeological response. *Water Resources Research*, *51*(2), 1300–1314. https://doi.org/10.1002/2014WR016168

Sättele, M., Bründl, M., & Straub, D. (2015). Reliability and effectiveness of early warning systems for natural hazards: Concept and application to debris flow warning. *Reliability Engineering & System Safety*, *142*, 192–202. https://doi.org/10.1016/j.ress.2015.05.003

Segoni, S., Piciullo, L., & Gariano, S. L. (2018). A review of the recent literature on rainfall thresholds for landslide occurrence. *Landslides*, *15*, 1483–1501. https://doi.org/10.1007/s10346-018-0966-4

Sempere-Torres, D., Porra, J. M., & Creutin, J.-D. (1994). A general formulation for raindrop size distribution. *Journal of Applied Meteorology and Climatology*, *33*, 1494–1502. https://doi.org/10.1175/1520-0450(1994)033⟨1494:AGFFRS⟩2.0.CO;2

Sideris, I. V., Gabella, M., Erdin, R., & Germann, U. (2014). Real-time radar-rain-gauge merging using spatio-temporal co-kriging with external drift in the alpine terrain of Switzerland. *Quarterly Journal of the Royal Meteorological Society*, *140*(680), 1097–1111. https://doi.org/10.1002/qj.2188

Simoni, A., Bernard, M., Berti, M., Boreggio, M., Lanzoni, S., Stancanelli, L., & Gregoretti, C. (2020). Runoff generated debris flows: Observation of initiation conditions and erosion deposition dynamics along the channel at Cancia (eastern Italian Alps). *Earth Surface Processes and Landforms*, *45*(14), 3556–3571. https://doi.org/10.1002/esp.4981

Sinclair, S., & Pegram, G. (2005). Combining radar and rain gauge rainfall estimates using conditional merging. *Atmospheric Science Letters*, *6*(1), 19–22. https://doi.org/10.1002/asl.85

Skinner, C., Bloetscher, F., & Pathak, C. S. (2009). Comparison of NEXRAD and rain gauge precipitation measurements in South Florida. *Journal of Hydrologic Engineering*, *14*(3), 248–260. https://doi.org/10.1061/(ASCE)1084-0699

Staley, D. M., Kean, J. W., Cannon, S. H., Schmidt, K. M., & Laber, J. L. (2013). Objective definition of rainfall intensity-duration thresholds for the initiation of post-fire debris flows in southern California. *Landslides*, *10*(5), 547–562. https://doi.org/10.1007/s10346-012-0341-9

Staley, D. M., Negri, J. A., Kean, J. W., Laber, J. L., Tillery, A. C., & Youberg, A. M. (2017). Prediction of spatially explicit rainfall intensityduration thresholds for post-fire debris-flow generation in the western United States. *Geomorphology*, *278*, 149–162. https://doi.org/10.1016/j.geomorph.2016.10.019

Stoffel, M., Tiranti, D., & Huggel, C. (2014). Climate change impacts on mass movements—Case studies from the European Alps. *Science of the Total Environment*, *493*, 1255–1266. https://doi.org/10.1016/j.scitotenv.2014.02.102

Tang, H., McGuire, L. A., Rengers, F. K., Kean, J. W., Staley, D. M., & Smith, J. B. (2019). Developing and testing physically based triggering thresholds for runoff-generated debris flows. *Geophysical Research Letters*, *46*(15), 8830–8839. https://doi.org/10.1029/2019GL083623

Tecca, P. R., & Genevois, R. (2009). Field observations of the June 30, 2001 debris flow at Acquabona (Dolomites, Italy). *Landslides*, *6*(1), 39–45. https://doi.org/10.1007/s10346-009-0145-8

Thiene, M., Shaw, W. D., & Scarpa, R. (2017). Perceived risks of mountain landslides in Italy: Stated choices for subjective risk reductions. *Landslides*, *14*(3), 1077–1089. https://doi.org/10.1007/s10346-016-0741-3

Tiranti, D., Cremonini, R., Marco, F., Gaeta, A. R., & Barbero, S. (2014). The DEFENSE (debris Flows triggEred by storms nowcasting system): An early warning system for torrential processes by radar storm tracking using a Geographic Information System (GIS). *Computers & Geosciences*, *70*, 96–109. https://doi.org/10.1016/j.cageo.2014.05.004

Tognacca, C., Bezzola, G. R., & Minor, H. E. (2000). Threshold criterion for debris-flow initiation due to channel-bed failure. In G. F. Wieczorek (Ed.), *Proceedings of the 2nd International Conference on Debris Flow, Hazards and Mitigation, Taipei/Taiwan* (pp. 89–97). Rotterdam: AA Balkema.

Tramblay, Y., Bouvier, C., Ayral, P.-A., & Marchandise, A. (2011). Impact of rainfall spatial distribution on rainfall-runoff modeling efficiency and initial soil moisture conditions estimation. *Natural Hazards and Earth System Sciences*, *11*(1), 157–170. https://doi.org/10.5194/nhess-11-157-2011

Tukey, J. W. (1977). *Exploratory data analysis* (1st ed.). Addison-Wesley Publishing Company.

Uhlenbrook, S., & Tetzlaff, D. (2006). Operational weather radar assessment of convective precipitation as an input to flood modeling in mountainous basins. In C. de Jong, D. Collins, & R. Ranzi (Eds.), *Climate and hydrology in mountain areas* (pp. 233–246). Chichester, UK: John Wiley & Sons. https://doi.org/10.1002/0470858249.ch16

Velasco-Forero, C. A., Sempere-Torres, D., Cassiraga, E. F., & Jaime Gómez-Hernández, J. (2009). A non-parametric automatic blending methodology to estimate rainfall fields from rain gauge and radar data. *Advances in Water Resources*, *32*(7), 986–1002. https://doi.org/10.1016/j.advwatres.2008.10.004

Verworn, A., & Haberlandt, U. (2011). Spatial interpolation of hourly rainfall effect of additional information, variogram inference and storm properties. *Hydrology and Earth System Sciences*, *15*(2), 569–584. https://doi.org/10.5194/hess-15-569-2011

Villarini, G., Mandapaka, P. V., Krajewski, W. F., & Moore, R. J. (2008). Rainfall and sampling uncertainties: A rain gauge perspective. *Journal of Geophysical Research*, *113*(D11), D11102. https://doi.org/10.1029/2007JD009214

Vogl, S., Laux, P., Qiu, W., Mao, G., & Kunstmann, H. (2012). Copula-based assimilation of radar and gauge information to derive bias-corrected precipitation fields. *Hydrology and Earth System Sciences*, *16*(7), 2311–2328. https://doi.org/10.5194/hess-16-2311-2012

Wei, Z.-l., Xu, Y.-P., Sun, H.-y., Xie, W., & Wu, G. (2018). Predicting the occurrence of channelized debris flow by an integrated cascading model: A case study of a small debris flow-prone catchment in Zhejiang Province, China. *Geomorphology*, *308*, 78–90. https://doi.org/10.1016/j.geomorph.2018.01.027

Wüest, M., Frei, C., Altenhoff, A., Hagen, M., Litschi, M., & Schär, C. (2010). A gridded hourly precipitation dataset for Switzerland using rain-gauge analysis and radar-based disaggregation. *International Journal of Climatology*, *30*(12), 1764–1775. https://doi.org/10.1002/joc.2025